bioRxiv preprint doi: https://doi.org/10.64898/2026.09.30.755482; this version posted October 18, 2026. The copyright holder for this preprint (which was not certified by peer review) is the author/funder, who has granted bioRxiv a license to display the preprint in perpetuity. It is made available under a CC-BY 4.0 International license.

Piezophilic activity dominates the Puerto Rico Trench deep subseafloor biosphere

Miguel Desmarais[1]*, Corinna Breusing[2], Anna H. Finch[3], Chloé M. J. Baumas[3], William D. Orsi[4], Alvaro M. Plominsky[1], Yuki Morono[5], Laura M. Wehrmann[6], Dennis Graham[2], Robert A. Pockalny[2], Arthur J. Spivack[2], Irita Aylward[8], Taylor Walton[8], Barbara Saucedo[1], Sofía Rivera Soto[7], Jelis Sostre-Cortes[7], Ying Zhang[9], Evan A. Solomon[8], David C. Smith[2], Anne E. Dekas[3], Jeffrey S. Bowman[1], Steven D'Hondt[2] and Douglas H. Bartlett[1]*

[1] Scripps Institution of Oceanography, University of California San Diego, La Jolla, CA, USA

[2] Graduate School of Oceanography, University of Rhode Island, Narragansett, RI, USA

[3] Department of Earth System Science, Stanford University, Stanford, CA, USA

[4] Department of Earth and Environmental Sciences, Ludwig-Maximilians-Universität München, Munich, Germany

[5] Kochi Institute for Core Sample Research, Japan Agency for Marine-Earth Science and Technology, Nankoku, Kochi, Japan

[6] School of Marine and Atmospheric Sciences, Stony Brook University, Stony Brook, NY, USA

[7] University of Puerto Rico at Mayagüez, Mayagüez, Puerto Rico, USA

[8] School of Oceanography, University of Washington, Seattle, WA, USA

[9] Department of Cell and Molecular Biology, University of Rhode Island, Kingston, RI, USA

*Corresponding authors: mdesmarais@ucsd.edu; dbartlett@ucsd.edu

bioRxiv preprint doi: https://doi.org/10.64898/2026.09.30.755482; this version posted October 18, 2026. The copyright holder for this preprint (which was not certified by peer review) is the author/funder, who has granted bioRxiv a license to display the preprint in perpetuity. It is made available under a CC-BY 4.0 International license.

Abstract

Hydrostatic pressure defines the deep ocean, yet its role in structuring microbial activity across the subseafloor biosphere remains poorly understood. Here, we assessed pressure effects on anabolic activity in sediment communities across margin-proximal, bathyal, abyssal, and hadal settings of the Puerto Rico Trench (493–8,385 m water depth). Community-level responses to pressure reversed with burial, revealing an unrecognized shift toward piezophily in communities down to 20 meters below seafloor (mbsf). Atmospheric pressure yielded higher proportions of active cells in surficial sediments, whereas *in situ* pressure yielded higher proportions in the subseafloor. Pressure also structured active-community composition; in trench-axis sediments down to 8.35 mbsf, JS1/Atribacterota populations within widespread hadal lineages exhibited a physiological response to *in situ* pressure, indicative of subseafloor piezophily. These findings suggest that hydrostatic pressure acts as an ecological filter after burial, favoring piezophilic traits that may support microbial persistence in the deep subseafloor biosphere.

bioRxiv preprint doi: https://doi.org/10.64898/2026.09.30.755482; this version posted October 18, 2026. The copyright holder for this preprint (which was not certified by peer review) is the author/funder, who has granted bioRxiv a license to display the preprint in perpetuity. It is made available under a CC-BY 4.0 International license.

The subseafloor biosphere hosts microbial life extending kilometers below the seafloor[1,2]. Although cell abundance and metabolic rates generally decline with burial, microorganisms remain active under severe energy limitation over geological timescales[1,3,4]. Hydrostatic pressure increases with water depth by approximately 1 MPa per 100 m, reaching 110 MPa (>1,000 atmospheres) in the deepest trenches, constraining microbial physiology and activity throughout the deep ocean[5–9]. Yet pressure is frequently excluded from experimental studies of the subseafloor biosphere owing to the technical challenges of conducting experiments under *in situ* pressure[10].

Pressure has been shown to structure microbial community composition and diverse biogeochemical processes in deep-ocean environments, including organic matter degradation and carbon, nitrogen, and sulfur cycling[5,10–15]. In surficial deep-sea sediments, community-level responses to pressure range from piezosensitive responses, characterized by lower microbial activity when exposed to pressures above atmospheric pressure (*i.e.*, >0.1 MPa), to piezophilic responses, characterized by higher microbial activity when exposed to elevated pressure (>10 MPa)[8,9]. Early experiments with surficial Puerto Rico Trench-axis sediments showed strong piezosensitivity, with bulk heterotrophic activity suppressed under *in situ* pressure[16]. In contrast, activity in abyssal Atlantic sediments was maintained or enhanced, indicating pressure tolerance or piezophily[17,18]. Below the sediment surface, however, evidence for piezophily is largely limited to a small number of microorganisms isolated from deep subseafloor sediments [19–21]. Community-level responses to pressure after burial remain largely unknown, including the extent to which pressure acts as an ecological filter shaping microbial persistence over geological timescales.

bioRxiv preprint doi: https://doi.org/10.64898/2026.09.30.755482; this version posted October 18, 2026. The copyright holder for this preprint (which was not certified by peer review) is the author/funder, who has granted bioRxiv a license to display the preprint in perpetuity. It is made available under a CC-BY 4.0 International license.

Hadal trenches provide a natural setting in which to address this knowledge gap. Their steep bathymetry creates pronounced hydrostatic-pressure gradients across relatively short geographic distances. Topographic focusing and episodic mass wasting also generate heterogeneous depositional environments and sedimentary records[22–24]. These gradients can extend from margin-proximal to hadal environments in trenches adjacent to continental margins, providing a natural framework for examining microbial pressure responses across hydrostatic regimes and sediment burial depths.

Here, we experimentally assessed community-level responses to pressure across sediment depths ranging from the seafloor surface to 20 meters below the seafloor (mbsf) in the Puerto Rico Trench region (493–8,385 m water depth). Bioorthogonal non-canonical amino acid tagging (BONCAT) was used to compare the proportion of anabolically active cells in natural communities incubated without added complex organic growth substrates under atmospheric and *in situ* pressure. Stable-isotope tracing and nanoscale secondary ion mass spectrometry (nanoSIMS) provided complementary single-cell measurements in surficial trench-axis sediments. Fluorescence-activated cell sorting (FACS), metagenomics, and comparative phylogenomics were used to resolve the populations underlying these pressure responses. Together, these approaches reveal a reversal in microbial pressure responses with burial, from piezosensitivity at the sediment surface to piezophily in the subseafloor, and link this response to widespread hadal JS1/Atribacterota lineages.

bioRxiv preprint doi: https://doi.org/10.64898/2026.09.30.755482; this version posted October 18, 2026. The copyright holder for this preprint (which was not certified by peer review) is the author/funder, who has granted bioRxiv a license to display the preprint in perpetuity. It is made available under a CC-BY 4.0 International license.

Results

To examine microbial pressure responses across an *in situ* hydrostatic pressure gradient, we investigated seven sites extending from the margin-proximal site PR02, across the bathyal slope (PR05 and PR04) and abyssal slope (PR06), to the hadal trench axis (PR07 and PR08) and adjacent abyssal plain (PR10) (Fig. 1a,b; Supplementary Table 1). These sites differed in organic matter content and composition, redox conditions, microbial biomass proxies and diversity, providing contrasting depositional and biogeochemical settings (Figs. 1c and 2).

Pressure effects on the proportion of anabolically active cells reverse with burial

We quantified the proportion of anabolically active cells using BONCAT in paired atmospheric- and *in situ*-pressure incubations of surficial and subsurface sediments (Figs. 3 and 4; Supplementary Table 8). Responses yielding higher proportions of anabolically active cells under atmospheric or *in situ* pressure were classified as piezosensitive or piezophilic, respectively, following the activity-based pressure-response framework of Amano et al.[5]. Across all incubations, BONCAT-positive cells comprised 0.4–56.8% of cells.

In surficial sediments, the proportion of BONCAT-positive cells under *in situ* pressure decreased with increasing water depth, from approximately 22% at the shallowest site (PR02; 493 meters below sea level [mbsl]) to <2% at the hadal trench-axis sites PR07 and PR08 (8,359–8,385 mbsl) ($\rho = -0.93$, $P = 0.0025$, $n = 7$ sites; Fig. 3b). Among the four sites with paired atmospheric and *in situ* pressure treatments (PR02, PR04, PR10 and

bioRxiv preprint doi: https://doi.org/10.64898/2026.09.30.755482; this version posted October 18, 2026. The copyright holder for this preprint (which was not certified by peer review) is the author/funder, who has granted bioRxiv a license to display the preprint in perpetuity. It is made available under a CC-BY 4.0 International license.

PR07), mean proportions of BONCAT-positive cells were 1.2–6.1-fold higher under atmospheric pressure, with the greatest differences at sites PR10 and PR07. The Pressure Activity Index (PAI), calculated from mean BONCAT-positive proportions as (*in situ* − atmospheric)/(*in situ* + atmospheric), became increasingly negative across the *in situ* pressure gradient along the transect, reaching −0.72 at PR10 (54 MPa) and −0.70 at PR07 (84 MPa; Fig. 3c).

In contrast, all six subsurface horizons yielded 1.3–3.7-fold higher mean BONCAT-positive proportions under *in situ* pressure across margin-proximal, bathyal-slope, hadal trench-axis and abyssal-plain sediments (PR02, PR05, PR04, PR07 and PR10; Fig. 4a; Supplementary Table 8). PAI values were consistently positive (0.13–0.57), demonstrating a reversal in pressure response with burial (Fig. 4b).

Atmospheric pressure *enhances single-cell anabolic activity in surficial sediment at trench-axis PR07*

We independently assessed surficial BONCAT-derived piezosensitivity using nanoSIMS measurements of single-cell ^{15}N-ammonium and ^{13}C-bicarbonate assimilation at PR07 and PR08. At PR07, median ^{15}N atom percent excess (APE) among ^{15}N-active cells was higher under atmospheric (0.0792) than *in situ* pressure (0.0710) in cell-level comparisons of single incubations (adjusted $P = 4.13 \times 10^{-5}$; Fig. 3f; Supplementary Table 9). At PR08, the cell-level distributions did not differ between pressure treatments (adjusted $P = 1.00$). Nevertheless, atmospheric-pressure incubations at both sites showed broader ^{15}N APE distributions and greater cell-to-cell heterogeneity than *in situ*-pressure incubations, with extended upper tails particularly apparent at PR08 (Supplementary

bioRxiv preprint doi: https://doi.org/10.64898/2026.09.30.755482; this version posted October 18, 2026. The copyright holder for this preprint (which was not certified by peer review) is the author/funder, who has granted bioRxiv a license to display the preprint in perpetuity. It is made available under a CC-BY 4.0 International license.

Table 9). In contrast, ^{13}C-bicarbonate assimilation was negligible across pressure treatments at both sites (Supplementary Table 9).

Active microbial populations differ between pressure *regimes in trench-axis sediments*

To identify populations underlying pressure responses at trench-axis PR07, BONCAT-positive cells from both pressure treatments were isolated and sequenced using fluorescence-activated cell sorting (BONCAT-FACS-seq). Libraries contained 211–3,078 sorted cells per fraction, and genera detected in the sequenced negative control were excluded (Supplementary Table 10). In surficial sediment, *Omnitrophus* dominated the *in situ*-pressure fraction (93.6% of Bracken-estimated genus-level reads), whereas *Pseudomonas* dominated under atmospheric pressure (79.3%), with a smaller contribution from *Psychrobacter*. In subsurface sediments (417–427 and 825–835 cmbsf), *in situ*-pressure fractions were dominated by JS1/Atribacterota, primarily the Genome Taxonomy Database (GTDB) placeholder taxon 34-128 (90–96%), whereas atmospheric-pressure fractions were dominated by *Acinetobacter* (82.8% and 99.9%, respectively), with smaller contributions from *Pseudomonas*. Previous studies reported atmospheric-pressure activity and piezosensitivity among hadal *Pseudomonas* and *Psychrobacter*[25,26]. However, *Pseudomonas* and *Acinetobacter* are potential low-biomass contaminants despite their absence from the reagent-only control, and secondary growth cannot be excluded[27,28], precluding further physiological interpretation. In both subsurface horizons, *in situ*-pressure BONCAT-positive communities more closely resembled unincubated communities (T_0) than atmospheric-pressure communities, based

bioRxiv preprint doi: https://doi.org/10.64898/2026.09.30.755482; this version posted October 18, 2026. The copyright holder for this preprint (which was not certified by peer review) is the author/funder, who has granted bioRxiv a license to display the preprint in perpetuity. It is made available under a CC-BY 4.0 International license.

on Bray–Curtis dissimilarity (Supplementary Table 10). Similarity to T_0 under *in situ* pressure was greater in the subsurface than at the surface.

To identify resident active populations, BONCAT-FACS-seq reads were recruited to the dereplicated T_0 metagenome-assembled genome (MAG) collection. No surficial BONCAT-FACS-seq reads, including those assigned to *Omnitrophus*, recruited to the available MAG collection, potentially reflecting incomplete genomic representation of active surficial populations. Prolonged incubations may also have introduced community selection alongside physiological responses. At both subsurface horizons, JS1 MAGs within the GTDB 34-128 lineage accounted for 53.9% and 64.0% of MAG relative abundance in *in situ*-pressure BONCAT-positive fractions at 417–427 and 825–835 cmbsf, respectively (Supplementary Table 11). Reads from below-threshold (B-T) fractions also recruited to these JS1 MAGs, indicating that these populations included cells both below and above the BONCAT-positive fluorescence threshold. High-confidence recruitment identified resident JS1 MAGs associated with anabolic activity under *in situ* pressure: PRT_8359_394_Bin36 and PRT_8359_709_Bin1 at 417–427 cmbsf, and PRT_8359_394_Bin36 at 825–835 cmbsf.

Organic matter and redox structure vary across depositional settings

To contextualize pressure-dependent activity, we examined relationships among organic matter properties, redox conditions, and microbial biomass across the transect. Total organic carbon (TOC) content was generally higher at the margin-proximal site PR02 (0.40–0.80 wt.%), intermediate at PR05, PR06 and PR10, and lowest at PR04 (0.02–0.22 wt.%), whereas the highest individual TOC values occurred in deeper horizons at the

bioRxiv preprint doi: https://doi.org/10.64898/2026.09.30.755482; this version posted October 18, 2026. The copyright holder for this preprint (which was not certified by peer review) is the author/funder, who has granted bioRxiv a license to display the preprint in perpetuity. It is made available under a CC-BY 4.0 International license.

hadal trench-axis sites PR07 and PR08 (up to 0.94 wt.%; Figs. 1c and 2b; Supplementary Table 2). Bulk organic carbon isotopic composition (δ^{13}Corg) was relatively ^{13}C-enriched at PR02 and PR05 (−23.3 to −19.0‰), generally intermediate at PR04, PR06 and PR10 (−28.2 to −22.4‰), with occasional strongly ^{13}C-depleted values, and consistently more ^{13}C-depleted in the lower TOC-rich intervals at the hadal trench-axis sites PR07 and PR08 (−27.7 to −23.5‰; Extended Data Fig. 1a; Supplementary Table 2).

Sites PR07 and PR08 exhibited an upper carbonate-rich interval and a lower TOC-rich, ^{13}C-depleted interval separated at 425 and 575 centimeters below seafloor (cmbsf), respectively (Fig. 1c; Supplementary Table 2). The upper interval contained high $CaCO_3$ content (up to 78.6 wt.%), moderate TOC content (0.18–0.54 wt.%) and relatively ^{13}C-enriched organic carbon (δ^{13}Corg, −24.2 to −22.2‰), whereas the lower interval contained low $CaCO_3$ content (0.4–1.9 wt.%), higher TOC content (0.77–0.94 wt.%) and more ^{13}C-depleted organic carbon (−27.7 to −27.1‰; Fig. 2a; Extended Data Fig. 2; Supplementary Table 2).

Across the full dataset, TOC content was strongly negatively correlated with oxygen concentration ($\rho = -0.71$, $P < 2.2 \times 10^{-16}$; Fig. 2c; Supplementary Table 4), whereas $\delta^{13}C_{org}$ showed a weaker negative correlation ($\rho = -0.35$, $P = 2.37 \times 10^{-4}$; Supplementary Table 4). Oxygen penetration was shallower at PR02, PR05, PR07 and PR08 than at PR04, PR06 and PR10 (Extended Data Fig. 1c; Supplementary Table 3). It broadly decreased with increasing TOC content but differed among intermediate-TOC sites, being shallower at PR05 than at the more ^{13}C-depleted PR06 and PR10.

bioRxiv preprint doi: https://doi.org/10.64898/2026.09.30.755482; this version posted October 18, 2026. The copyright holder for this preprint (which was not certified by peer review) is the author/funder, who has granted bioRxiv a license to display the preprint in perpetuity. It is made available under a CC-BY 4.0 International license.

Biomass and diversity covary with organic matter properties

Cell abundance, total adenylate (ATP + ADP + AMP), and rarefied amplicon sequence variant (ASV) richness generally remained elevated downcore at sites PR02, PR05, PR07 and PR08 relative to PR04, PR06 and PR10 (Fig. 1c; Extended Data Fig. 1e,g; Supplementary Tables 5–7). Across the transect, TOC correlated positively with total adenylate ($\rho = 0.48$, $P = 4.97 \times 10^{-4}$) and rarefied ASV richness ($\rho = 0.56$, $P = 1.47 \times 10^{-6}$), but its relationship with cell abundance was weaker and not statistically significant ($\rho = 0.33$, $P = 0.0584$; Fig. 2d–f). δ^{13}Corg correlated positively with cell abundance ($\rho = 0.48$, $P = 0.014$), total adenylate ($\rho = 0.48$, $P = 8.3 \times 10^{-4}$) and rarefied ASV richness ($\rho = 0.56$, $P = 6.8 \times 10^{-8}$; Extended Data Fig. 3j–l; Supplementary Table 4). Thus, TOC captured broad variation in microbial biomass-linked and diversity proxies, while $\delta^{13}C_{org}$ tracked contrasting biological and redox conditions among sites with similar TOC.

TOC content decouples from microbial biomass and richness in subseafloor ^{13}C-depleted trench sediments

Despite higher TOC content, cell abundance, total adenylate, and ASV richness in the lower TOC-rich, ^{13}C-depleted intervals at PR07 and PR08 fell below their transect-wide relationships with TOC (Fig. 2d–f). Averaged across sediment samples from PR07 and PR08 within each interval, total adenylate concentration decreased from 9.44×10^{-4} to 4.24×10^{-4} nM, and rarefied ASV richness decreased from 1,571 to 1,432 ASVs from the upper carbonate-rich to the lower TOC-rich, ^{13}C-depleted intervals. In contrast, subsurface cell abundance remained relatively stable across this transition (Extended

bioRxiv preprint doi: https://doi.org/10.64898/2026.09.30.755482; this version posted October 18, 2026. The copyright holder for this preprint (which was not certified by peer review) is the author/funder, who has granted bioRxiv a license to display the preprint in perpetuity. It is made available under a CC-BY 4.0 International license.

Data Fig. 1e; Supplementary Table 5). Adenylate content normalized to cell abundance also decreased across this transition (Extended Data Fig. 1f; Supplementary Table 7).

Distinct JS1 populations are enriched in hadal trench-axis sediments

16S rRNA gene profiles and MAG distributions revealed differences in JS1/Atribacterota abundance and clade composition among PR05, PR07 and PR08 (Fig. 5d; Supplementary Table 12). Three dominant 99%-clustered JS1-16S clades (1–3) showed clear bathyal–hadal partitioning. At PR05, JS1-16S clade 3 predominated and total JS1 abundance remained low (0–14.11% of 16S reads), whereas trench-axis PR07 and PR08 were dominated by JS1-16S clades 1 and 2, reaching downcore maxima of 77.03% and 76.63%, respectively. This bathyal–hadal pattern was reflected among four representative Puerto Rico Trench JS1 MAGs: the two *in situ*-pressure-active MAGs at PR07 were present at low relative abundance at PR05 but became increasingly abundant downcore at PR07 and PR08 (Fig. 6c).

JS1 abundance was highest within the lower TOC-rich, ^{13}C-depleted intervals at PR07 and PR08 (Fig. 5c,d). Across JS1-containing sites (PR05, PR07 and PR08), JS1 relative abundance increased with TOC ($\rho = 0.76$, adjusted $P < 0.001$) and sediment depth ($\rho = 0.53$, adjusted $P < 0.001$), and decreased with oxygen ($\rho = -0.77$, adjusted $P < 0.001$) and $\delta^{13}C_{org}$ ($\rho = -0.56$, adjusted $P = 0.002$; Supplementary Table 13).

In situ-pressure-active JS1 belong to hadal-associated phylogenomic clades

Phylogenomic analysis of Puerto Rico Trench and geographically distant JS1 genomes resolved two hadal-associated clades spanning the Puerto Rico, Atacama, Japan,

bioRxiv preprint doi: https://doi.org/10.64898/2026.09.30.755482; this version posted October 18, 2026. The copyright holder for this preprint (which was not certified by peer review) is the author/funder, who has granted bioRxiv a license to display the preprint in perpetuity. It is made available under a CC-BY 4.0 International license.

Kermadec and Mariana trenches (Fig. 6b,e; Supplementary Table 14). These lineages, designated JS1 hadal clades A and B, belonged to GTDB taxon 34-128 (Atribacterota, class JS1) and were distinct from non-hadal upper-slope and bathyal JS1 genomes. Pairwise average amino acid identity (AAI) comparisons placed most JS1 genome pairs, including comparisons between hadal clades A and B, within the genus-like range, whereas species-like values were restricted to subsets within each clade (Extended Data Fig. 6).

The two JS1 MAGs to which reads from *in situ*-pressure BONCAT-positive fractions were recruited belonged to the hadal-associated clades: PRT_8359_709_Bin1 in hadal clade A and PRT_8359_394_Bin36 in hadal clade B (Fig. 6b). In contrast, two representative JS1 MAGs recovered from the shallower PR05 site, PRT_1902_744_Bin5 and PRT_1902_593_Bin9, fell outside the hadal-associated clades and did not recruit reads from *in situ*-pressure BONCAT-positive fractions (Fig. 6b; Supplementary Table 11).

Hadal-associated JS1 clades are genomically differentiated

KEGG Ortholog (KO)-based functional profiles differentiated JS1 phylogenomic groups, with hadal clade B showing the strongest separation from non-hadal genomes and clade A occupying a region closer to sedimentary organic-matter-associated non-hadal JS1 (Fig. 6d). KO-based functional profiles differed among JS1 genomic groups even after accounting for the carbon/substrate regime of their source environments (*e.g.,* methane- versus organic matter-dominated; PERMANOVA, genomic group $R^2 = 0.156$, P =

bioRxiv preprint doi: https://doi.org/10.64898/2026.09.30.755482; this version posted October 18, 2026. The copyright holder for this preprint (which was not certified by peer review) is the author/funder, who has granted bioRxiv a license to display the preprint in perpetuity. It is made available under a CC-BY 4.0 International license.

252 0.0001), although multivariate dispersion also differed among groups (P = 0.0003; Fig.
253 6d; Supplementary Table 15).

254 Clade B had the highest median predicted proteome-wide charged-residue fraction
255 (27.62%), significantly exceeding both clade A (26.99%) and non-hadal genomes
256 (27.29%), and these differences remained significant after accounting for genome
257 completeness, contamination and genome recovery type (Fig. 6d; Supplementary Tables
258 16 and 17). Clade B also had a significantly higher KO-assigned open reading frame
259 (ORF) fraction than clade A after accounting for these factors (Supplementary Table 17).

260

bioRxiv preprint doi: https://doi.org/10.64898/2026.09.30.755482; this version posted October 18, 2026. The copyright holder for this preprint (which was not certified by peer review) is the author/funder, who has granted bioRxiv a license to display the preprint in perpetuity. It is made available under a CC-BY 4.0 International license.

Discussion

Here we report a reversal in microbial responses to hydrostatic pressure with burial across the Puerto Rico Trench region, from predominantly piezosensitive surficial communities to piezophilic subsurface communities. This reversal occurred across contrasting depositional settings, revealing piezophily as a recurring physiological feature of the subseafloor communities examined here. In subsurface hadal trench-axis sediments, dominant JS1/Atribacterota populations belonging to geographically widespread hadal lineages showed a strong response to *in situ* pressure, indicative of piezophily.

In surficial sediment at trench-axis site PR07, a community-level piezosensitive response was supported by both a higher proportion of anabolically active cells and greater ammonium assimilation among ^{15}N-active cells under atmospheric relative to *in situ* pressure (Fig. 3b,c,f). Negligible ^{13}C-bicarbonate assimilation across pressure treatments was consistent with heterotrophy predominating during the incubation period (Fig. 3f). This pattern mirrors early observations from surficial Puerto Rico Trench-axis sediments, where heterotrophic uptake and cellular assimilation of ^{14}C-labeled amino acids were strongly suppressed at *in situ* relative to atmospheric pressure[16]. At the community level, such net pressure responses reflect the relative abundance and activity of pressure-sensitive and pressure-adapted populations[9]. Accordingly, continual delivery of particle-associated microorganisms with limited prior pressure exposure may sustain pressure-sensitive populations in surficial sediments across the transect, potentially enhanced by topographic focusing at the trench axis[15,22–24,29,30]. Consistent with this interpretation, the

bioRxiv preprint doi: https://doi.org/10.64898/2026.09.30.755482; this version posted October 18, 2026. The copyright holder for this preprint (which was not certified by peer review) is the author/funder, who has granted bioRxiv a license to display the preprint in perpetuity. It is made available under a CC-BY 4.0 International license.

283 magnitude of surficial PAI increased with water depth, paralleling evidence from deep-
284 water communities that increasing hydrostatic pressure progressively constrains
285 microbial activity, with implications for estimates of carbon cycling at depth[5]. At PR07,
286 greater cell-to-cell heterogeneity among ^{15}N-active cells under atmospheric pressure
287 further suggests that a highly responsive, pressure-sensitive subset may contribute
288 disproportionately to the net pressure response (Fig. 3f)[31].

289 Below the sediment surface, PAI captured the opposite pattern: *in situ* pressure yielded
290 higher proportions of anabolically active cells across all six subsurface horizons
291 examined (Figs. 4a,b). The consistent shift from piezosensitive surface responses to
292 piezophilic responses after burial suggests that piezophilic physiology becomes
293 advantageous in the subsurface, favoring the persistence of pressure-adapted members of
294 subseafloor communities[9,12]. Sustained hydrostatic pressure over thousands to millions of
295 years may filter surface-derived populations during burial, consistent with observed
296 subseafloor community restructuring[32–34]. The present experiments cannot resolve
297 whether pressure-adapted populations primarily persisted after burial or proliferated
298 within the subsurface. However, the placement of pressure-active JS1 populations within
299 geographically widespread hadal-associated phylogenomic clades links the observed
300 physiological response to evolutionary differentiation among JS1 lineages. Together,
301 these observations are consistent with sustained hydrostatic pressure acting as an
302 ecological filter during burial.

303 Hydrostatic pressure also structured the taxonomic composition of the active fraction. At
304 trench-axis site PR07, *Omnitrophus* dominated the *in situ*-pressure-active fraction in

bioRxiv preprint doi: https://doi.org/10.64898/2026.09.30.755482; this version posted October 18, 2026. The copyright holder for this preprint (which was not certified by peer review) is the author/funder, who has granted bioRxiv a license to display the preprint in perpetuity. It is made available under a CC-BY 4.0 International license.

surficial sediment, while JS1/34-128 dominated the *in situ*-pressure-active fractions in both subsurface horizons. Neither was detected in the corresponding atmospheric-pressure-active fractions, consistent with piezophilic physiology in these populations (Fig. 5e; Extended Data Fig. 4d; Supplementary Tables 10 and 11). Active assemblages more closely resembled unincubated T_0 communities under atmospheric pressure at the surface and *in situ* pressure in the subsurface, suggesting that piezophilic physiology is embedded within the resident subseafloor community (Supplementary Table 10).

Recruitment of BONCAT-positive reads to resident T_0 MAGs further linked the subsurface pressure response to JS1/Atribacterota. Within this group, the piezophilic response was lineage-specific: genome-resolved populations active under *in situ* pressure at hadal PR07 were distinct from those characteristic of bathyal PR05. JS1-16S clades showed similar bathyal–hadal partitioning, consistent with ecological differentiation along the bathymetric gradient (Figs. 5d and 6b,c; Supplementary Tables 11 and 12). The pressure-active trench-axis populations belonged to hadal-associated phylogenomic clades spanning geographically distant trenches, raising the possibility that piezophilic physiology is widespread among hadal JS1 populations (Fig. 6b,e; Supplementary Table 14)[35–37]. Functional differentiation among JS1 genomic groups, strongest in hadal clade B, persisted after accounting for carbon/substrate regime, suggesting that hydrostatic pressure may contribute alongside other hadal environmental factors (Fig. 6d; Supplementary Table 15). Candidate traits for maintaining cellular function under pressure included an elevated charged-residue fraction in clade B and the genomic potential of Puerto Rico Trench JS1 MAGs to synthesize the compatible solutes trehalose and di-myo-inositol-phosphate, as identified in a separate study[38], although their

bioRxiv preprint doi: https://doi.org/10.64898/2026.09.30.755482; this version posted October 18, 2026. The copyright holder for this preprint (which was not certified by peer review) is the author/funder, who has granted bioRxiv a license to display the preprint in perpetuity. It is made available under a CC-BY 4.0 International license.

328 contributions to piezophily remain untested (Extended Data Fig. 7; Supplementary Tables
329 16 and 17)[39–41]. Previous studies have shown that JS1/Atribacterota are abundant and
330 transcriptionally active in deeply buried marine sediments, including evidence for
331 populations persisting over geological timescales[42,43]. Our findings provide evidence of
332 piezophilic physiology among particular JS1 populations belonging to evolutionarily
333 differentiated hadal lineages spanning geographically distant trenches, potentially
334 contributing to their ecological success in the subseafloor biosphere.

335 The exceptional enrichment of both hadal JS1 clades at the trench axis coincided with
336 sustained high pressure and distinctive depositional and energetic conditions. A
337 carbonate-rich upper interval overlay a TOC-rich lower interval with δ^{13}Corg reaching
338 −27.7‰, the most depleted value among surveyed hadal sediments (Fig. 5c; Extended
339 Data Fig. 1b; Supplementary Table 18). This succession may reflect episodic downslope
340 delivery of margin- or terrestrial-derived organic matter, consistent with a previously
341 identified regional debrite[22,23,44,45]. Despite high TOC, the lower interval supported
342 disproportionately low microbial standing stocks, adenylate content and diversity,
343 potentially reflecting organic matter source and lability alongside low anaerobic energy
344 yields (Figs. 1c and 2d–f; Extended Data Fig. 1e–g; Supplementary Tables 5–7)[44,46–48].
345 Yet JS1/Atribacterota comprised up to 77% of 16S reads, among the highest abundances
346 reported for marine sediments (Fig. 5d; Supplementary Tables 12 and 13)[35,40,49–51]. This
347 enrichment despite low microbial standing stocks suggests that JS1 populations may be
348 particularly well suited to persistence under these restrictive conditions. JS1 MAGs
349 encoded pathways for peptide and sugar fermentation and microcompartment-associated
350 secondary fermentation, potentially supporting energy conservation and persistence under

bioRxiv preprint doi: https://doi.org/10.64898/2026.09.30.755482; this version posted October 18, 2026. The copyright holder for this preprint (which was not certified by peer review) is the author/funder, who has granted bioRxiv a license to display the preprint in perpetuity. It is made available under a CC-BY 4.0 International license.

these conditions[35,40,42,51,52]. The recurrence and ecological prominence of hadal JS1 lineages across geographically distant trenches may therefore reflect ecological specialization to both sustained hydrostatic pressure and trench-specific depositional, redox, and energetic regimes[53].

Together, our findings identify hydrostatic pressure as a key determinant of microbial activity in marine sediments. Its effect reversed with burial, from piezosensitive responses at the sediment surface to piezophilic responses across contrasting subsurface settings, including sediments buried meters beneath the hadal trench axis. This reversal, together with the association of pressure-active JS1 populations with widespread hadal lineages, is consistent with the hypothesis that sustained pressure acts as an ecological filter over long timescales, favoring populations with piezophilic physiology. Because pressure altered the prevalence and taxonomic distribution of anabolic activity, *in situ*-pressure experiments are essential for constraining microbial contributions to sedimentary biogeochemical cycling. More broadly, our findings suggest that piezophilic physiology may be widespread in the deep subseafloor biosphere, providing a new perspective on microbial adaptation and persistence in one of Earth's largest microbial habitats.

bioRxiv preprint doi: https://doi.org/10.64898/2026.09.30.755482; this version posted October 18, 2026. The copyright holder for this preprint (which was not certified by peer review) is the author/funder, who has granted bioRxiv a license to display the preprint in perpetuity. It is made available under a CC-BY 4.0 International license.

Methods

Study area and sample collection

Sediment samples were collected from seven sites (PR02, PR04, PR05, PR06, PR07, PR08 and PR10) spanning margin, slope, hadal trench-axis and adjacent abyssal-plain settings of the Puerto Rico Trench region during cruise AR64-02 (15 February–10 March 2022) aboard the R/V *Neil Armstrong* (Fig. 1a,b; Supplementary Table 1). Sampling sites ranged from 493 to 8,385 meters below sea level (mbsl), corresponding to approximate *in situ* hydrostatic pressures of 5–84 MPa. Sediment cores were recovered using multicore, gravity-core and piston-core systems.

Recovered cores were sectioned into whole rounds on deck and maintained at 4 °C in a shipboard refrigerated van until subsampling. Core temperature was monitored upon recovery to minimize warming during retrieval and handling. Sediment subsamples were collected from the interior of each core section using sterile 60-mL cut-off syringes to minimize contamination from material in contact with the core liner and were subsequently processed or preserved according to downstream analyses.

Ancillary geochemical, biochemical, and molecular datasets

Geochemical, biochemical, and molecular datasets used in this study included dissolved oxygen (O_2), nitrate (NO_3^-), sulfate (SO_4^{2-}), TOC, total nitrogen (TN), $CaCO_3$, $\delta^{13}C_{org}$, total adenylate (ATP + ADP + AMP), 16S rRNA gene profiles, and sediment metagenomes. O_2, NO_3^-, and SO_4^{2-} concentrations were measured as previously

bioRxiv preprint doi: https://doi.org/10.64898/2026.09.30.755482; this version posted October 18, 2026. The copyright holder for this preprint (which was not certified by peer review) is the author/funder, who has granted bioRxiv a license to display the preprint in perpetuity. It is made available under a CC-BY 4.0 International license.

388 described by Fischer et al.[54]. Total organic carbon (TOC) content and δ^{13}Corg were
389 determined following the method described in Swenson Perger et al.[55] and Cohen et al.[56]
390 in the Department of Geosciences at Stony Brook University. TN and $CaCO_3$ were
391 measured as described by Trejos-Espeleta et al.[57]. Total adenylate was measured as
392 described by Orsi[58] and normalized to cell abundance where paired measurements were
393 available. Additionally, 16S rRNA gene profiles and the Puerto Rico Trench MAG
394 collection generated from field-collected, unincubated sediment samples were
395 incorporated from Breusing et al.[38]; metagenomic assembly, genome binning, quality
396 assessment, and dereplication are described therein.

397 *16S rRNA gene analysis and JS1 clade definition*

398 Previously generated 16S rRNA gene profiles from the broader Puerto Rico Trench
399 amplicon dataset (NCBI BioProject PRJNA1334354) were reanalyzed to evaluate depth
400 distributions of JS1-affiliated populations across PR05, PR07 and PR08[38]. JS1-affiliated
401 ASVs were extracted from the finalized ASV table, and per-sample relative abundances
402 were calculated from read counts normalized to total reads. To evaluate fine-scale JS1
403 population structure, JS1-affiliated sequence variants were clustered by pairwise
404 sequence similarity using VSEARCH at a 99% identity threshold[59]. The three dominant
405 99%-identity groups are referred to here as JS1-16S clades 1–3 to distinguish them from
406 genome-based hadal clades A and B.

bioRxiv preprint doi: https://doi.org/10.64898/2026.09.30.755482; this version posted October 18, 2026. The copyright holder for this preprint (which was not certified by peer review) is the author/funder, who has granted bioRxiv a license to display the preprint in perpetuity. It is made available under a CC-BY 4.0 International license.

Sediment cell separation

Microbial cells were separated from sediment using a workflow modified from Morono et al.[60]. The workflow was used for total cell enumeration of unincubated samples and downstream BONCAT and nanoSIMS analyses of incubated samples. Cell separation for total counts was performed at JAMSTEC, whereas BONCAT-associated extractions were performed at the Scripps Institution of Oceanography (SIO). Formaldehyde-fixed sediment slurry was combined with a chemical cell-detachment mixture containing 100 mM EDTA, 100 mM sodium pyrophosphate, 1% (v/v) Tween 80 and methanol and vortexed at high speed for 1 h. Samples were subsequently sonicated for 20 min in 30-s on/off cycles at 4 °C. A detailed protocol is available on protocols.io[61]. Samples processed at JAMSTEC were sonicated in an ice-cooled Bioruptor water bath (Diagenode, Seraing, Belgium) at 20 W, whereas samples processed at SIO were sonicated on ice using a Model 50 Sonic Dismembrator (Fisher Scientific, Waltham, MA, USA) at 20% power. Cell extracts were separated by density-gradient centrifugation over 30%, 50% and 80% Nycodenz layered above 80% (w/v) sodium polytungstate at 10,000 × *g* for 1 h at 4 °C. The recovered aqueous cell fraction was used for downstream analyses.

Total cell enumeration

For total cell counts, the recovered cell fraction was diluted 1:100, collected onto 0.2-µm polycarbonate filters, stained with 10× SYBR Green I in phosphate-buffered saline (PBS), and enumerated at JAMSTEC using an automated fluorescence microscopy system based on an Olympus BX-51 microscope (Olympus Corporation, Hachioji,

bioRxiv preprint doi: https://doi.org/10.64898/2026.09.30.755482; this version posted October 18, 2026. The copyright holder for this preprint (which was not certified by peer review) is the author/funder, who has granted bioRxiv a license to display the preprint in perpetuity. It is made available under a CC-BY 4.0 International license.

Tokyo, Japan) equipped with an automatic slide handler, LED illumination and a cooled CCD camera, following Morono et al. and Morono and Inagaki[60,62].

Pressure incubations

Before the cruise, artificial seawater (ASW) was prepared from Sea Salts (40 g L^{-1}; Sigma-Aldrich, St. Louis, MO, USA; pH ~7), amended with L-cysteine hydrochloride (0.5 g L^{-1}) as a reducing agent and resazurin (0.5 mg L^{-1}) as an oxygen indicator, aliquoted in 30-mL volumes into metalized polyethylene terephthalate pouches (IMPAK Corporation, Sebastian, FL, USA), flushed with ultra-high-purity N_2 and heat-sealed. The pre-aliquoted ASW was kept cold until sediment processing aboard ship. Pouches were then reopened under continuous N_2 flushing, and sediment slurry incubations were prepared by combining 30 mL of sediment with 30 mL of ASW (1:1, v/v). Sodium sulfide (150 µL of a 5% [w/v] stock solution; Sigma-Aldrich) was added as a reductant to maintain anoxic conditions. BONCAT incubations were amended with L-homopropargylglycine (HPG; Vector Laboratories, Newark, CA, USA; CCT-1067) to a final concentration of 50 µM, whereas stable-isotope incubations for nanoSIMS were amended with ^{13}C-bicarbonate (1.04 mM; Cambridge Isotope Laboratories, Tewksbury, MA, USA; CLM-441) and ^{15}N-ammonium (0.65 mM; Cambridge Isotope Laboratories; NLM-467). All shipboard manipulations were performed on ice using pre-chilled ASW, with sediment slurries continuously flushed with ultra-high-purity N_2 during processing to minimize oxygen exposure. Following addition of sediment and incubation amendments, pouches were homogenized and heat-sealed without headspace. An ASW-

bioRxiv preprint doi: https://doi.org/10.64898/2026.09.30.755482; this version posted October 18, 2026. The copyright holder for this preprint (which was not certified by peer review) is the author/funder, who has granted bioRxiv a license to display the preprint in perpetuity. It is made available under a CC-BY 4.0 International license.

only control was included with each pressure-treatment set to assess maintenance of anoxic conditions independently of the sediment incubation controls.

In situ-pressure incubations were conducted in custom pin-retained piston-closure pressure vessels filled with distilled water as the hydraulic medium[63]. Sealed incubation pouches were loaded into the vessels and pressurized to *in situ* hydrostatic pressure using an eTensifier electric high-pressure pump system (High Pressure Equipment Company [HiP], Erie, PA, USA). For the shallowest site (PR02; 493 m water depth), the surface sediment incubation was conducted at 8.5 MPa, the minimum pressure achievable with the pressure intensifier, rather than the approximately 5 MPa corresponding to the sampling depth. Pressure was measured using the eTensifier integrated pressure transducer. For BONCAT, each sample included two HPG-amended replicates and one HPG-free sediment negative control at *in situ* pressure, with a parallel set maintained at atmospheric pressure. Both atmospheric pressure and *in situ* pressure incubations were maintained at 4 °C for the remainder of the cruise. Pressurized vessels were transported under pressure in a refrigerated van to Scripps Institution of Oceanography, where incubation continued at 4 °C for a total incubation period of 10 weeks to permit detectable HPG incorporation in low-activity deep-sediment communities. Vessel pressure was verified using the eTensifier immediately before depressurization and subsampling at the end of the incubation period. ASW-only controls were opened in an anaerobic chamber and inspected for resazurin color change to verify maintenance of anoxic conditions.

bioRxiv preprint doi: https://doi.org/10.64898/2026.09.30.755482; this version posted October 18, 2026. The copyright holder for this preprint (which was not certified by peer review) is the author/funder, who has granted bioRxiv a license to display the preprint in perpetuity. It is made available under a CC-BY 4.0 International license.

After incubation, pouches were opened in an anaerobic chamber (Coy Laboratory Products, Grass Lake, MI, USA), and matching 5-mL slurry aliquots were collected for downstream analyses. Aliquots for BONCAT and nanoSIMS activity measurements were fixed overnight at 4 °C with formaldehyde at a final concentration of 4%, washed with PBS and 1:1 PBS:ethanol, and preserved in ethanol. Unfixed aliquots for BONCAT-FACS-seq were preserved separately in glycine-TE buffer.

BONCAT single-cell activity measurements

Extracted cells were prestained with SYBR Green I in solution, collected onto 25-mm, 0.2-µm polycarbonate filters, and washed twice with 3 mL of 1× PBS before on-filter click chemistry following the general framework of Couradeau et al.[64]; a detailed protocol is available at protocols.io[65]. The click-reaction mixture contained 100 µM $CuSO_4$, 500 µM THPTA, 5 µM Cy5 azide dye (Vector Laboratories, Newark, CA, USA), 5 mM sodium ascorbate, and 5 mM aminoguanidine-HCl in 1× PBS. Filters were incubated with 80 µL of click-reaction mixture for 30 min in the dark under a coverslip. After labeling, filters were washed three times with 3 mL of 1× PBS, cut into quarters, and one quarter was mounted on glass slides in VECTASHIELD mounting medium; the remaining filter material was preserved at −80 °C.

Mounted filter quarters were imaged on a SLIDEVIEW VS200 fluorescence microscope (Olympus Corporation, Hachioji, Japan) using FITC and Cy5 filter sets: FITC/SYBR Green, Ex 474/27 nm, dichroic 495 nm, Em 525/45 nm; and Cy5, Ex 635/18 nm, dichroic 652 nm, Em 680/42 nm. For each replicate filter, a large-area scan covering most of one mounted quarter was acquired and analyzed in QuPath[66]. Total cells were identified from

bioRxiv preprint doi: https://doi.org/10.64898/2026.09.30.755482; this version posted October 18, 2026. The copyright holder for this preprint (which was not certified by peer review) is the author/funder, who has granted bioRxiv a license to display the preprint in perpetuity. It is made available under a CC-BY 4.0 International license.

493 the SYBR Green/FITC channel using the Cell Detection tool, and BONCAT-positive
494 cells were identified from Cy5 fluorescence using a single-image object classifier.
495 Corresponding HPG-free negative controls were carried through labeling and imaging
496 and used to define background Cy5 fluorescence and BONCAT-positive classification
497 thresholds, which were held constant across replicate images within each sample and
498 treatment. Counts of total and BONCAT-positive cells were used to calculate the
499 proportion of anabolically active cells. Pressure effects were summarized using a
500 normalized Pressure Activity Index (PAI), adapted from the pressure-effect metric (Pe) of
501 Tamburini et al.[9]. PAI was calculated from the mean proportion of BONCAT-positive
502 cells across the two incubation replicates for each treatment as (*in situ* − atmospheric)/(*in*
503 *situ* + atmospheric), with positive and negative values indicating greater activity under *in*
504 *situ* and atmospheric pressure, respectively.

505 *NanoSIMS single-cell activity measurements*

506 Fixed cells collected on gold-coated filters were mounted on conductive carbon tabs on
507 glass slides and analyzed using a NanoSIMS 50L (CAMECA, Gennevilliers, France) at
508 the nano@stanford facility. Randomly selected areas were pre-sputtered over 40 × 40 µm
509 for 2 min, after which 30 × 30 µm areas were analyzed with a 5-pA Cs^+ primary ion
510 beam, a 200-µm aperture (D1-3), and a 256 × 256-pixel raster across 40 serial images.
511 An entrance slit of 20 × 140 µm (ES-3) and aperture slit of 80 × 80 µm (AS-4) were used.
512 Secondary ions were collected for $^{12}C^-$, $^{13}C^-$, $^{12}C^{12}C^-$, $^{12}C^{13}C^-$, $^{12}C^{14}N^-$ and $^{12}C^{15}N^-$. Mass
513 resolving power was approximately 9,000 as reported by the CAMECA software.

bioRxiv preprint doi: https://doi.org/10.64898/2026.09.30.755482; this version posted October 18, 2026. The copyright holder for this preprint (which was not certified by peer review) is the author/funder, who has granted bioRxiv a license to display the preprint in perpetuity. It is made available under a CC-BY 4.0 International license.

Regions of interest (ROIs) that were interpreted as cells were manually delineated in Look@nanoSIMS[67] using carbon-, nitrogen- and isotope-ratio images. Between 194 and 377 ROIs were analyzed per sample; ROIs with Poisson error >10% were excluded. Incubations were amended with both ^{13}C-bicarbonate and ^{15}N-ammonium, and incorporation of both isotopes was evaluated. A T_0 sample consisting of PR10 sediment fixed immediately after addition of stable-isotope-labeled substrates was used as a common baseline for calculating atom percent excess (APE) and defining thresholds for detectable ^{13}C and ^{15}N enrichment, with immediate fixation minimizing biological incorporation of the added tracers. Daily measurements were adjusted by one-point correction to a check standard. Cells were classified as ^{13}C- or ^{15}N-active when their respective atom fraction exceeded the corresponding T_0 mean by >2 standard deviations, and APE was calculated as described by Pett-Ridge and Weber[68].

BONCAT-FACS, genome amplification, and sequencing

To recover DNA from anabolically active cell populations, sediment slurries from three PR07 horizons (0–10, 417–427 and 825–835 cmbsf) were analyzed by BONCAT-FACS-seq. Slurries were incubated with HPG for 10 weeks and subsequently preserved in glycine-TE buffer. Samples were processed using the cell extraction, on-filter DNA staining and BONCAT click-chemistry labeling workflow described above, with Alexa Fluor 405 azide dye (Vector Laboratories, Newark, CA, USA) used as the BONCAT fluorophore and with modifications to preserve cell integrity for sorting. Specifically, the sonication step used during standard cell extraction was omitted, and after labeling and

bioRxiv preprint doi: https://doi.org/10.64898/2026.09.30.755482; this version posted October 18, 2026. The copyright holder for this preprint (which was not certified by peer review) is the author/funder, who has granted bioRxiv a license to display the preprint in perpetuity. It is made available under a CC-BY 4.0 International license.

535 washing, cells were gently resuspended from filters into 1× PBS containing 0.02%
536 Tween 20 for flow cytometric sorting[15].

537 Cell populations were sorted on a BD FACSDiscover S8 Cell Sorter (BD Biosciences,
538 Franklin Lakes, NJ, USA) at the Scripps Research Flow Cytometry Core Facility.
539 Instrument performance and optical alignment were verified using the facility's standard
540 quality-control and calibration procedures before sample acquisition and sorting. SYBR
541 Green fluorescence was excited by the 488-nm blue laser and detected in the B3 channel
542 (532/16-nm bandpass), while red fluorescence was excited by the 640-nm red laser and
543 detected in the R2 channel (675/20-nm bandpass). These fluorescence parameters,
544 together with forward and side scatter, were used to distinguish cellular particles from
545 sediment particles and background events. Within the gated cell population, Alexa Fluor
546 405 fluorescence (V3 [460]-A) was used to separate HPG-labeled BONCAT-positive
547 cells from the B-T fraction. An HPG-amended copper-omission click-chemistry control
548 prepared from PR02 surficial sediment (0–10 cmbsf; 8.5 MPa) was used to characterize
549 background Alexa Fluor 405 fluorescence and define the BONCAT-positive sorting
550 threshold. A reagent-only PBS control containing the processing reagents in PBS but no
551 sediment-derived cells was carried through BONCAT-FACS separately, and events
552 within the sort gate were collected for downstream MDA and sequencing to identify
553 reagent- and workflow-associated contaminants. Cells within the parent-cell gate were
554 sorted into a BONCAT-positive fraction and a separate below-threshold fraction
555 comprising cells that did not exceed the Alexa Fluor 405 fluorescence threshold used for
556 BONCAT-positive sorting. The same gates were applied consistently across samples.
557 Sorting was performed in purity mode into low-bind tubes containing PBS. Sample-

bioRxiv preprint doi: https://doi.org/10.64898/2026.09.30.755482; this version posted October 18, 2026. The copyright holder for this preprint (which was not certified by peer review) is the author/funder, who has granted bioRxiv a license to display the preprint in perpetuity. It is made available under a CC-BY 4.0 International license.

specific acquired-event counts, sorted-cell counts, sequencing results and read-QC summaries are provided in Supplementary Table 10.

Because sorted-cell biomass was low, cells were lysed and genomic DNA was amplified using the REPLI-g Single Cell Kit (QIAGEN, Hilden, Germany; cat. no. 150343) according to the manufacturer's single-cell protocol. Following cell lysis and DNA denaturation/neutralization, Phi29 polymerase-based multiple displacement amplification (MDA) was performed at 30 °C for 8 h, followed by polymerase inactivation at 65 °C for 3 min. The reagent-only PBS control was carried through MDA and sequencing alongside the sorted experimental fractions. Accordingly, BONCAT-FACS-seq profiles were interpreted as the taxonomic composition of recovered, detectably labeled cells rather than as quantitative estimates of total-community composition. Amplified DNA was submitted to the DNA Technologies and Expression Analysis Core at the UC Davis Genome Center for Illumina library preparation and sequencing on an Illumina NovaSeq X platform using 2 × 150 bp paired-end sequencing. Sequencing and read-QC summaries are provided in Supplementary Table 10.

BONCAT-FACS-seq bioinformatic analysis

Raw BONCAT-FACS-seq reads were assessed using FastQC v0.12.1[69] and adapter- and quality-trimmed using Trimmomatic v0.39[70] with the parameters ILLUMINACLIP:TruSeq3-PE-2.fa:2:30:10, LEADING:3, TRAILING:3, SLIDINGWINDOW:4:15 and MINLEN:36. Post-trimming read quality was assessed using FastQC and summarized using MultiQC v1.19[71]. Taxonomic classification was performed using Kraken2 v2.14[72] against a custom GTDB release 226 database

bioRxiv preprint doi: https://doi.org/10.64898/2026.09.30.755482; this version posted October 18, 2026. The copyright holder for this preprint (which was not certified by peer review) is the author/funder, who has granted bioRxiv a license to display the preprint in perpetuity. It is made available under a CC-BY 4.0 International license.

580 downsampled to a maximum hash-table size of 128 GB using the Kraken2 --max-db-size
581 option, with a classification confidence threshold of 0.05. Taxonomic abundances were
582 estimated using Bracken v3.1[73] with a read length of 150 bp and a minimum abundance
583 threshold of 10 reads; genus-level profiles were used for downstream community-
584 composition analyses. Genera detected in the sequenced reagent-only PBS control were
585 removed. Relative abundances were recalculated from the retained Bracken-estimated
586 reads after contaminant filtering. Bray–Curtis dissimilarity between each sorted fraction
587 and its corresponding T_0 metagenomic community was calculated from the resulting
588 genus-level relative-abundance profiles after normalization to unit sum.

589 For genome-resolved recruitment, quality-controlled paired-end reads were mapped
590 against the Puerto Rico Trench MAG collection[38] (NCBI BioProject PRJNA1334354)
591 using Bowtie2 v2.5.4[74] with the --very-sensitive-local setting, retaining a single best
592 alignment per read (-k 1) and allowing insert sizes up to 2,000 bp. Primary alignments
593 were processed using SAMtools v1.20[75], with unmapped, secondary, and supplementary
594 alignments excluded and a minimum mapping quality of 20. MAG recruitment and
595 genome coverage were quantified using CoverM v0.7.0, retaining alignments with ≥95%
596 nucleotide identity across ≥75% of the read. MAG–sample pairs with ≥20% genome
597 breadth of coverage were classified as high-confidence recruitment; remaining non-zero
598 recruitment was considered low-level.

599 *Phylogenomic analysis*

600 JS1-affiliated MAGs and single amplified genomes (SAGs) from marine sediments were
601 compiled from published studies, associated NCBI genome repositories, and genomes

bioRxiv preprint doi: https://doi.org/10.64898/2026.09.30.755482; this version posted October 18, 2026. The copyright holder for this preprint (which was not certified by peer review) is the author/funder, who has granted bioRxiv a license to display the preprint in perpetuity. It is made available under a CC-BY 4.0 International license.

provided directly by principal investigators when available (Supplementary Table 14). Genome quality was assessed with CheckM v1[76], and taxonomy was assigned with GTDB-Tk using GTDB release 226[77] to confirm placement within the JS1 class-level lineage. Genomes were retained for phylogenomic analysis if they had ≥50% completeness and <10% contamination based on CheckM estimates. Genomes yielding all-gap marker alignments were excluded from downstream tree construction. Environmental source metadata for each genome were obtained from the corresponding publication and, where available, associated NCBI metadata. Prior to comparative genomic analysis, sampling environments were manually classified into broader carbon/substrate regimes based on the reported depositional setting and substrate characteristics; genome-specific assignments and source metadata are provided in Supplementary Table 14.

Phylogenomic reconstruction was performed with the non-dereplicated MAG/SAG collection so that closely related genomes were retained and fine-scale lineage structure could be visualized. Conserved bacterial single-copy marker genes were identified and concatenated with GToTree v1.6.31 using the built-in bacterial HMM set in best-hit mode[78]. Maximum-likelihood phylogenies were inferred from the concatenated protein alignment using IQ-TREE[79], with ModelFinder used to select the best-fit substitution model[80] and branch support assessed with 1,000 ultrafast bootstrap replicates[81]. The final tree was visualized and annotated in iTOL v7.6[82]. Pairwise AAI was calculated from predicted protein sets using CompareM v0.1.2 to evaluate genome-relatedness within and between JS1 clades. AAI values of 65–95% and ≥95% were interpreted as approximate

bioRxiv preprint doi: https://doi.org/10.64898/2026.09.30.755482; this version posted October 18, 2026. The copyright holder for this preprint (which was not certified by peer review) is the author/funder, who has granted bioRxiv a license to display the preprint in perpetuity. It is made available under a CC-BY 4.0 International license.

624 genus-like and species-like similarity ranges, respectively, following commonly used
625 genome-relatedness thresholds[83].

626 *Genome architecture, functional annotation, and physicochemical properties*

627 Genome architecture metrics were calculated for the retained JS1 MAG/SAG set using
628 CheckM v1.2.5 and Prodigal v2.6.3. Outputs included observed genome size, corrected
629 genome size, GC content, predicted ORF count, and predicted ORF density[76,84].
630 Corrected genome size was calculated as observed genome size × 100 / (completeness −
631 contamination), and ORF density was calculated as predicted ORFs per corrected Mbp.
632 Predicted proteins were assigned to KOs using KOfamScan v1.3.0[85].

633 Proteome physicochemical properties were calculated from Prodigal-predicted proteins
634 using the Peptides package[86]. Genome-level proteome summaries included protein
635 isoelectric point, acidic:basic residue ratio, charged residue fraction, hydrophobic residue
636 fraction, and amino-acid composition. Genome architecture, KO-assignment, and
637 proteome physicochemical metrics were summarized for non-hadal JS1 genomes and
638 hadal-associated JS1 clades resolved in the phylogenomic analysis.

639 *Statistical analyses*

640 Statistical analyses were performed in R v4.5.3, with multivariate analyses conducted
641 using vegan v2.7-5[87]. BONCAT-positive proportions were measured in two incubation
642 replicates per sediment horizon and pressure treatment and were therefore compared
643 descriptively using replicate values, fold differences between treatment means, and PAI.

bioRxiv preprint doi: https://doi.org/10.64898/2026.09.30.755482; this version posted October 18, 2026. The copyright holder for this preprint (which was not certified by peer review) is the author/funder, who has granted bioRxiv a license to display the preprint in perpetuity. It is made available under a CC-BY 4.0 International license.

644 The relationship between water depth and the mean *in situ*-pressure BONCAT-positive
645 proportion in surficial sediments was tested using a two-sided Spearman rank correlation
646 across the seven sites.

647 Cellular isotope-incorporation analyses were restricted to isotopically enriched ("active")
648 ROIs interpreted as cells because sediment background prevented reliable identification
649 and enumeration of all unenriched cells in the $^{12}C^{14}N^-$ and $^{12}C^{12}C^-$ images. Cellular ^{15}N
650 atom percent excess distributions were compared between pressure treatments within
651 each site using two-sided Wilcoxon rank-sum tests with Bonferroni correction for two
652 comparisons. Because each site and pressure treatment comprised one nanoSIMS
653 incubation, these tests compare cell-level distributions within incubations and do not
654 represent incubation-level replication. Gini coefficients were calculated separately from
655 ^{13}C and ^{15}N APE values of active cells using DescTools v0.99.60 to quantify cell-to-cell
656 heterogeneity in isotope assimilation[31].

657 Associations among geochemical variables, biomass-linked proxies, rarefied ASV
658 richness and JS1 relative abundance were tested using two-sided Spearman rank
659 correlations. Variables measured at different sediment depths were paired within sites
660 using maximum-cardinality, minimum-total-offset one-to-one matching without
661 replacement; matching tolerances and median depth offsets are reported in
662 Supplementary Table 4. O_2 was linearly interpolated to target horizons and set to zero at
663 and below the first measured zero. The 15 transect-wide correlations were adjusted
664 together using the Benjamini–Hochberg procedure. Correlations between JS1 relative

bioRxiv preprint doi: https://doi.org/10.64898/2026.09.30.755482; this version posted October 18, 2026. The copyright holder for this preprint (which was not certified by peer review) is the author/funder, who has granted bioRxiv a license to display the preprint in perpetuity. It is made available under a CC-BY 4.0 International license.

abundance and geochemical variables constituted a separate analysis family and were adjusted separately using the Benjamini–Hochberg procedure (Supplementary Table 13).

Group-wise comparisons among non-hadal JS1 genomes and the two hadal-associated clades were performed using pairwise Wilcoxon rank-sum tests, with *P* values adjusted for multiple comparisons using the Benjamini–Hochberg procedure (Supplementary Table 16). These tests were applied to genome architecture metrics, KO-assignment metrics and predicted proteome physicochemical properties. Because genome type and quality differed among JS1 genomic groups (Extended Data Fig. 5), covariate-adjusted linear models were used as robustness checks for selected genome architecture, KO-assignment and proteome physicochemical metrics. These models included JS1 group as the predictor of interest and CheckM-estimated completeness, CheckM-estimated contamination and genome type as covariates. Statistical outputs are reported in Supplementary Table 17.

Multivariate differences in KO-based functional profiles were assessed using Bray–Curtis dissimilarities calculated from KO copy densities normalized per 1,000 predicted proteins. Ordination was performed by principal coordinate analysis (PCoA), and group differences were tested using PERMANOVA with adonis2 in vegan, with additional models including carbon/substrate regime as a covariate. Differences in multivariate dispersion were evaluated using betadisper in vegan. Statistical outputs are reported in Supplementary Table 15.

bioRxiv preprint doi: https://doi.org/10.64898/2026.09.30.755482; this version posted October 18, 2026. The copyright holder for this preprint (which was not certified by peer review) is the author/funder, who has granted bioRxiv a license to display the preprint in perpetuity. It is made available under a CC-BY 4.0 International license.

685 References

686 1. Parkes, R. J. *et al.* Deep bacterial biosphere in Pacific Ocean sediments. *Nature* **371**,
687 410–413 (1994).
688 2. Kallmeyer, J., Pockalny, R., Adhikari, R. R., Smith, D. C. & D'Hondt, S. Global
689 distribution of microbial abundance and biomass in subseafloor sediment. *Proc. Natl.*
690 *Acad. Sci.* **109**, 16213–16216 (2012).
691 3. D'Hondt, S. *et al.* Distributions of microbial activities in deep subseafloor sediments.
692 *Science* **306**, 2216–2221 (2004).
693 4. Hoehler, T. M. & Jørgensen, B. B. Microbial life under extreme energy limitation.
694 *Nat Rev Microbiol* **11**, 83–94 (2013).
695 5. Amano, C. *et al.* Limited carbon cycling due to high-pressure effects on the deep-sea
696 microbiome. *Nat. Geosci.* **15**, 1041–1047 (2022).
697 6. Bartlett, D. H. Pressure effects on in vivo microbial processes. *Biochim. Biophys.*
698 *Acta* **1595**, 367–381 (2002).
699 7. Lauro, F. M. & Bartlett, D. H. Prokaryotic lifestyles in deep sea habitats.
700 *Extremophiles* **12**, 15–25 (2008).
701 8. Scoma, A. Functional groups in microbial ecology: updated definitions of piezophiles
702 as suggested by hydrostatic pressure dependence on temperature. *ISME J.* **15**, 1871–
703 1878 (2021).
704 9. Tamburini, C., Boutrif, M., Garel, M., Colwell, R. R. & Deming, J. W. Prokaryotic
705 responses to hydrostatic pressure in the ocean – a review. *Env. Microbiol* **15**, 1262–
706 1274 (2013).

bioRxiv preprint doi: https://doi.org/10.64898/2026.09.30.755482; this version posted October 18, 2026. The copyright holder for this preprint (which was not certified by peer review) is the author/funder, who has granted bioRxiv a license to display the preprint in perpetuity. It is made available under a CC-BY 4.0 International license.

10. Garel, M. *et al.* Pressure-Retaining Sampler and High-Pressure Systems to Study Deep-Sea Microbes Under *in situ* Conditions. *Front. Microbiol.* **10**, 453 (2019).
11. Bowles, M. W., Samarkin, V. A. & Joye, S. B. Improved measurement of microbial activity in deep-sea sediments at *in situ* pressure and methane concentration. *Limnol. Oceanogr. Methods* **9**, 499–506 (2011).
12. Vossmeyer, A., Deusner, C., Kato, C., Inagaki, F. & Ferdelman, T. Substrate-specific pressure-dependence of microbial sulfate reduction in deep-sea cold seep sediments of the Japan Trench. *Front. Microbiol.* **3**, (2012).
13. Stief, P. *et al.* Hydrostatic pressure induces transformations in the organic matter and microbial community composition of marine snow particles. *Commun. Earth Environ.* **4**, 377 (2023).
14. Lloyd, C. C., Balmonte, J. P., Glud, R. N. & Arnosti, C. Strong Effects of Increased Hydrostatic Pressure on Polysaccharide-Hydrolyzing Enzyme Activities in Coastal Seawater and Sediments. *J. Geophys. Res. Biogeosciences* **130**, e2024JG008417 (2025).
15. Plominsky, A. M. *et al.* Minimizing decompression and warming during deep seawater collection increases abundance and activity of autochthonous bacteria and archaea. *ISME J.* **20**, wrag064 (2026).
16. Schwarz, J. R. & Colwell, R. R. Heterotrophic Activity of Deep-Sea Sediment Bacteria. *Appl. Microbiol.* **30**, 639–649 (1975).
17. Tabor, P. S., Deming, J. W., Ohwada, K. & Colwell, R. R. Activity and growth of microbial populations in pressurized deep-sea sediment and animal gut samples. *Appl. Environ. Microbiol.* **44**, 413–422 (1982).

bioRxiv preprint doi: https://doi.org/10.64898/2026.09.30.755482; this version posted October 18, 2026. The copyright holder for this preprint (which was not certified by peer review) is the author/funder, who has granted bioRxiv a license to display the preprint in perpetuity. It is made available under a CC-BY 4.0 International license.

730 18. Deming, J. W. & Colwell, R. R. Observations of Barophilic Microbial Activity in
731 Samples of Sediment and Intercepted Particulates from the Demerara Abyssal Plain.
732 *Appl. Environ. Microbiol.* **50**, 1002–1006 (1985).
733 19. Bale, S. J. *et al. Desulfovibrio profundus* sp. nov., a novel barophilic sulfate-reducing
734 bacterium from deep sediment layers in the Japan Sea. *Int. J. Syst. Bacteriol.* **47**,
735 515–521 (1997).
736 20. Fang, J. *et al.* Predominance of Viable Spore-Forming Piezophilic Bacteria in High-
737 Pressure Enrichment Cultures from ~1.5 to 2.4 km-Deep Coal-Bearing Sediments
738 below the Ocean Floor. *Front. Microbiol.* **8**, (2017).
739 21. Parkes, R. J., Cragg, B. A., Bale, S. J., Goodman, K. & Fry, J. C. A combined
740 ecological and physiological approach to studying sulphate reduction within deep
741 marine sediment layers. *J. Microbiol. Methods* **23**, 235–249 (1995).
742 22. Turnewitsch, R. *et al.* Recent sediment dynamics in hadal trenches: Evidence for the
743 influence of higher-frequency (tidal, near-inertial) fluid dynamics. *Deep Sea Res.*
744 *Part Oceanogr. Res. Pap.* **90**, 125–138 (2014).
745 23. Kioka, A. *et al.* Megathrust earthquake drives drastic organic carbon supply to the
746 hadal trench. *Sci. Rep.* **9**, 1553 (2019).
747 24. Oguri, K. *et al.* Sediment Accumulation and Carbon Burial in Four Hadal Trench
748 Systems. *J. Geophys. Res. Biogeosciences* **127**, e2022JG006814 (2022).
749 25. Yanagibayashi, M., Nogi, Y., Li, L. & Kato, C. Changes in the microbial community
750 in Japan Trench sediment from a depth of 6292 m during cultivation without
751 decompression. *FEMS Microbiol. Lett.* **170**, 271–279 (1999).

bioRxiv preprint doi: https://doi.org/10.64898/2026.09.30.755482; this version posted October 18, 2026. The copyright holder for this preprint (which was not certified by peer review) is the author/funder, who has granted bioRxiv a license to display the preprint in perpetuity. It is made available under a CC-BY 4.0 International license.

752 26. Peoples, L. M. *et al.* Vertically distinct microbial communities in the Mariana and
753 Kermadec trenches. *PLOS ONE* **13**, e0195102 (2018).
754 27. Salter, S. J. *et al.* Reagent and laboratory contamination can critically impact
755 sequence-based microbiome analyses. *BMC Biol.* **12**, 87 (2014).
756 28. Fierer, N. *et al.* Guidelines for preventing and reporting contamination in low-
757 biomass microbiome studies. *Nat. Microbiol.* **10**, 1570–1580 (2025).
758 29. Luo, M. *et al.* Sources, Degradation, and Transport of Organic Matter in the New
759 Britain Shelf-Trench Continuum, Papua New Guinea. *J. Geophys. Res.*
760 *Biogeosciences* **124**, 1680–1695 (2019).
761 30. Stief, P., Elvert, M. & Glud, R. N. Respiration by “marine snow” at high hydrostatic
762 pressure: Insights from continuous oxygen measurements in a rotating pressure tank.
763 *Limnol. Oceanogr.* **66**, 2797–2809 (2021).
764 31. Arandia-Gorostidi, N., Parada, A. E. & Dekas, A. E. Single-cell view of deep-sea
765 microbial activity and intracommunity heterogeneity. *ISME J.* **17**, 59–69 (2023).
766 32. Starnawski, P. *et al.* Microbial community assembly and evolution in subseafloor
767 sediment. *Proc. Natl. Acad. Sci.* **114**, 2940–2945 (2017).
768 33. D’Hondt, S., Pockalny, R., Fulfer, V. M. & Spivack, A. J. Subseafloor life and its
769 biogeochemical impacts. *Nat. Commun.* **10**, 3519 (2019).
770 34. Marshall, I. P. G. *et al.* Environmental filtering determines family-level structure of
771 sulfate-reducing microbial communities in subsurface marine sediments. *ISME J.* **13**,
772 1920–1932 (2019).
773 35. Jitsuno, K. *et al.* Comparative single-cell genomics of Atribacterota JS1 in the Japan
774 Trench hadal sedimentary biosphere. *mSphere* **9**, e00337-23 (2024).

bioRxiv preprint doi: https://doi.org/10.64898/2026.09.30.755482; this version posted October 18, 2026. The copyright holder for this preprint (which was not certified by peer review) is the author/funder, who has granted bioRxiv a license to display the preprint in perpetuity. It is made available under a CC-BY 4.0 International license.

36. Li, Y., Liu, H., Xiao, Y. & Jing, H. Metagenome sequencing and 982 microbial genomes from Kermadec and Diamantina Trenches sediments. *Sci. Data* **11**, 1067 (2024).

37. Schauberger, C. *et al.* Metagenome-assembled genomes of deep-sea sediments: changes in microbial functional potential lag behind redox transitions. *ISME Commun.* **4**, ycad005 (2024).

38. Breusing, C. *et al.* Seafloor topography structures subseafloor microbial communities in the Puerto Rico Trench. Preprint at https://doi.org/10.64898/2026.10.13.758824 (2026).

39. Peoples, L. M. *et al.* Distinctive gene and protein characteristics of extremely piezophilic Colwellia. *BMC Genomics* **21**, 692 (2020).

40. Glass, J. B. *et al.* Microbial metabolism and adaptations in *Atribacteria*-dominated methane hydrate sediments. *Environ. Microbiol.* **23**, 4646–4660 (2021).

41. Caliò, A. *et al.* Unravelling the Adaptation Mechanisms to High Pressure in Proteins. *Int. J. Mol. Sci.* **23**, 8469 (2022).

42. Bird, J. T. *et al.* Uncultured Microbial Phyla Suggest Mechanisms for Multi-Thousand-Year Subsistence in Baltic Sea Sediments. *mBio* **10**, e02376-18 (2019).

43. Vuillemin, A. *et al.* Atribacteria Reproducing over Millions of Years in the Atlantic Abyssal Subseafloor. *mBio* **11**, e01937-20 (2020).

44. Meyers, P. A. Preservation of elemental and isotopic source identification of sedimentary organic matter. *Chem. Geol.* **114**, 289–302 (1994).

bioRxiv preprint doi: https://doi.org/10.64898/2026.09.30.755482; this version posted October 18, 2026. The copyright holder for this preprint (which was not certified by peer review) is the author/funder, who has granted bioRxiv a license to display the preprint in perpetuity. It is made available under a CC-BY 4.0 International license.

45. Seibert, C. *et al.* Late Pleistocene charcoal-rich sediments in the Puerto Rico Trench, possible remnants of gigantic wildfires in North-Eastern South America. *Palaeogeogr. Palaeoclimatol. Palaeoecol.* **655**, 112497 (2024).

46. Burdige, D. J. Preservation of Organic Matter in Marine Sediments: Controls, Mechanisms, and an Imbalance in Sediment Organic Carbon Budgets? *Chem. Rev.* **107**, 467–485 (2007).

47. Bradley, J. A., Arndt, S., Amend, J. P., Burwicz-Galerne, E. & LaRowe, D. E. Sources and Fluxes of Organic Carbon and Energy to Microorganisms in Global Marine Sediments. *Front. Microbiol.* **13**, 910694 (2022).

48. Chu, M. *et al.* Sediment-modulated seafloor residence time controls efficient organic carbon burial in subduction zones. *Nat. Commun.* **17**, 5834 (2026).

49. Inagaki, F. *et al.* Biogeographical distribution and diversity of microbes in methane hydrate-bearing deep marine sediments on the Pacific Ocean Margin. *Proc. Natl. Acad. Sci.* **103**, 2815–2820 (2006).

50. Carr, S. A., Orcutt, B. N., Mandernack, K. W. & Spear, J. R. Abundant Atribacteria in deep marine sediment from the Adélie Basin, Antarctica. *Front. Microbiol.* **6**, (2015).

51. Lee, Y. M. *et al.* Genomic Insight Into the Predominance of Candidate Phylum Atribacteria JS1 Lineage in Marine Sediments. *Front. Microbiol.* **9**, 2909 (2018).

52. Nobu, M. K. *et al.* Phylogeny and physiology of candidate phylum 'Atribacteria' (OP9/JS1) inferred from cultivation-independent genomics. *ISME J.* **10**, 273–286 (2016).

bioRxiv preprint doi: https://doi.org/10.64898/2026.09.30.755482; this version posted October 18, 2026. The copyright holder for this preprint (which was not certified by peer review) is the author/funder, who has granted bioRxiv a license to display the preprint in perpetuity. It is made available under a CC-BY 4.0 International license.

53. Lv, Y. *et al.* Redox-stratified macromolecule degradation supports microbial survival in the oligotrophic Kermadec Trench sediments. *Nat. Commun.* **17**, 10138 (2026).

54. Fischer, J. P., Ferdelman, T. G., D'Hondt, S., Røy, H. & Wenzhöfer, F. Oxygen penetration deep into the sediment of the South Pacific gyre. *Biogeosciences* **6**, 1467–1478 (2009).

55. Swenson Perger, D. A. *et al.* Seasonal iron fluxes and iron cycling in sandy bioirrigated sediments. *Front. Mar. Sci.* **10**, 1293893 (2023).

56. Cohen, A. B. *et al.* Preserved particulate organic carbon is likely derived from the subsurface sulfidic photic zone of the Proterozoic Ocean: evidence from a modern, oxygen-deficient lake. *Geobiology* **22**, e12593 (2024).

57. Trejos-Espeleta, J. C. *et al.* Principal role of fungi in soil carbon stabilization during early pedogenesis in the high Arctic. *Proc. Natl. Acad. Sci.* **121**, e2402689121 (2024).

58. Orsi, W. D. A rapid method for measuring ATP + ADP + AMP in marine sediment. *Environ. Microbiol.* **25**, 1549–1558 (2023).

59. Rognes, T., Flouri, T., Nichols, B., Quince, C. & Mahé, F. VSEARCH: a versatile open source tool for metagenomics. *PeerJ* **4**, e2584 (2016).

60. Morono, Y., Terada, T., Kallmeyer, J. & Inagaki, F. An improved cell separation technique for marine subsurface sediments: applications for high-throughput analysis using flow cytometry and cell sorting. *Environ. Microbiol.* **15**, 2841–2849 (2013).

61. Desmarais, M. *Extraction of Microbial Cells from Marine Sediments for BONCAT Fluorescence Microscopy*. (2026) doi:10.17504/protocols.io.q2lydz1dwlx9/v1.

bioRxiv preprint doi: https://doi.org/10.64898/2026.09.30.755482; this version posted October 18, 2026. The copyright holder for this preprint (which was not certified by peer review) is the author/funder, who has granted bioRxiv a license to display the preprint in perpetuity. It is made available under a CC-BY 4.0 International license.

62. Morono, Y. & Inagaki, F. Automatic Slide-Loader Fluorescence Microscope for Discriminative Enumeration of Subseafloor Life. *Sci. Drill.* **9**, 32–36 (2010).

63. Marietou, A. & Bartlett, D. H. Effects of High Hydrostatic Pressure on Coastal Bacterial Community Abundance and Diversity. *Appl Env. Microbiol* **80**, 5992–6003 (2014).

64. Couradeau, E. *et al.* Probing the active fraction of soil microbiomes using BONCAT-FACS. *Nat Commun* **10**, 2770 (2019).

65. Desmarais, M. & Plominsky, A. M. *BONCAT-Based Quantification of Anabolically Active Microbial Cells in Marine Sediments by Fluorescence Microscopy*. (2026) doi:10.17504/protocols.io.byl42er22vo5/v1.

66. Bankhead, P. *et al.* QuPath: Open source software for digital pathology image analysis. *Sci. Rep.* **7**, 16878 (2017).

67. Polerecky, L. *et al.* Look@NanoSIMS – a tool for the analysis of nanoSIMS data in environmental microbiology. *Environ. Microbiol.* **14**, 1009–1023 (2012).

68. Pett-Ridge, J. & Weber, P. K. NanoSIP: NanoSIMS Applications for Microbial Biology. in *Microbial Systems Biology* (ed. Navid, A.) vol. 881 375–408 (Humana Press, Totowa, NJ, 2012).

69. Andrews, S. FastQC: A Quality Control Tool for High Throughput Sequence Data. Babraham Bioinformatics (2010).

70. Bolger, A. M., Lohse, M. & Usadel, B. Trimmomatic: a flexible trimmer for Illumina sequence data. *Bioinformatics* **30**, 2114–2120 (2014).

bioRxiv preprint doi: https://doi.org/10.64898/2026.09.30.755482; this version posted October 18, 2026. The copyright holder for this preprint (which was not certified by peer review) is the author/funder, who has granted bioRxiv a license to display the preprint in perpetuity. It is made available under a CC-BY 4.0 International license.

861 71. Ewels, P., Magnusson, M., Lundin, S. & Käller, M. MultiQC: summarize analysis
862 results for multiple tools and samples in a single report. *Bioinformatics* **32**, 3047–
863 3048 (2016).
864 72. Wood, D. E., Lu, J. & Langmead, B. Improved metagenomic analysis with Kraken 2.
865 *Genome Biol.* **20**, 257 (2019).
866 73. Lu, J., Breitwieser, F. P., Thielen, P. & Salzberg, S. L. Bracken: estimating species
867 abundance in metagenomics data. *PeerJ Comput. Sci.* **3**, e104 (2017).
868 74. Langmead, B. & Salzberg, S. L. Fast gapped-read alignment with Bowtie 2. *Nat.*
869 *Methods* **9**, 357–359 (2012).
870 75. Danecek, P. *et al.* Twelve years of SAMtools and BCFtools. *GigaScience* **10**, giab008
871 (2021).
872 76. Parks, D. H., Imelfort, M., Skennerton, C. T., Hugenholtz, P. & Tyson, G. W.
873 CheckM: assessing the quality of microbial genomes recovered from isolates, single
874 cells, and metagenomes. *Genome Res.* **25**, 1043–1055 (2015).
875 77. Chaumeil, P.-A., Mussig, A. J., Hugenholtz, P. & Parks, D. H. GTDB-Tk: a toolkit to
876 classify genomes with the Genome Taxonomy Database. *Bioinformatics* **36**, 1925–
877 1927 (2020).
878 78. Lee, M. D. GToTree: a user-friendly workflow for phylogenomics. *Bioinformatics*
879 **35**, 4162–4164 (2019).
880 79. Nguyen, L.-T., Schmidt, H. A., Von Haeseler, A. & Minh, B. Q. IQ-TREE: A Fast
881 and Effective Stochastic Algorithm for Estimating Maximum-Likelihood
882 Phylogenies. *Mol. Biol. Evol.* **32**, 268–274 (2015).

bioRxiv preprint doi: https://doi.org/10.64898/2026.09.30.755482; this version posted October 18, 2026. The copyright holder for this preprint (which was not certified by peer review) is the author/funder, who has granted bioRxiv a license to display the preprint in perpetuity. It is made available under a CC-BY 4.0 International license.

883 80. Kalyaanamoorthy, S., Minh, B. Q., Wong, T. K. F., Von Haeseler, A. & Jermiin, L.
884 S. ModelFinder: fast model selection for accurate phylogenetic estimates. *Nat.*
885 *Methods* **14**, 587–589 (2017).
886 81. Hoang, D. T., Chernomor, O., Von Haeseler, A., Minh, B. Q. & Vinh, L. S.
887 UFBoot2: Improving the Ultrafast Bootstrap Approximation. *Mol. Biol. Evol.* **35**,
888 518–522 (2018).
889 82. Letunic, I. & Bork, P. Interactive Tree Of Life (iTOL) v5: an online tool for
890 phylogenetic tree display and annotation. *Nucleic Acids Res.* **49**, W293–W296
891 (2021).
892 83. Konstantinidis, K. T., Rosselló-Móra, R. & Amann, R. Uncultivated microbes in need
893 of their own taxonomy. *ISME J.* **11**, 2399–2406 (2017).
894 84. Hyatt, D. *et al.* Prodigal: prokaryotic gene recognition and translation initiation site
895 identification. *BMC Bioinformatics* **11**, 119 (2010).
896 85. Aramaki, T. *et al.* KofamKOALA: KEGG Ortholog assignment based on profile
897 HMM and adaptive score threshold. *Bioinformatics* **36**, 2251–2252 (2020).
898 86. Osorio, D., Rondón-Villarreal, P. & Torres, R. Peptides: A Package for Data Mining
899 of Antimicrobial Peptides. *R J.* **7**, 4 (2015).
900 87. Oksanen, J. *et al.* vegan: Community Ecology Package.
901 https://doi.org/10.32614/CRAN.package.vegan (2001).
902
903

bioRxiv preprint doi: https://doi.org/10.64898/2026.09.30.755482; this version posted October 18, 2026. The copyright holder for this preprint (which was not certified by peer review) is the author/funder, who has granted bioRxiv a license to display the preprint in perpetuity. It is made available under a CC-BY 4.0 International license.

Acknowledgements

We thank the captain, crew, and scientific party of the R/V *Neil Armstrong* cruise AR64-02 for sample collection and shipboard support. We also thank undergraduate volunteers in the Bartlett laboratory at the Scripps Institution of Oceanography for assistance with sample processing and laboratory work. Cell extraction and enumeration were performed at the Kochi Institute for Core Sample Research, Japan Agency for Marine-Earth Science and Technology (JAMSTEC). Microscopy imaging was performed at the UC San Diego School of Medicine Microscopy Core, supported by NIH grants NS047101, OD030505, and OD036455. Part of this work was performed at nano@stanford RRID:SCR_026695. We thank Matthew Mills and Christie Jilly for assistance with nanoSIMS operation. Sequencing was carried out at the DNA Technologies and Expression Analysis Cores at the UC Davis Genome Center (RRID:SCR_017740), supported by NIH Shared Instrumentation Grant 1S10OD010786-01. Fluorescence-activated cell sorting was performed at the Scripps Research Flow Cytometry Core. We thank Gregory Henkes and Yang Gao for assistance with TOC and $\delta^{13}C_{org}$ analyses.

bioRxiv preprint doi: https://doi.org/10.64898/2026.09.30.755482; this version posted October 18, 2026. The copyright holder for this preprint (which was not certified by peer review) is the author/funder, who has granted bioRxiv a license to display the preprint in perpetuity. It is made available under a CC-BY 4.0 International license.

Funding

This work, including ship time, sample collection, analytical materials, and partial stipend support for M.D., was supported by the National Science Foundation (OCE-2049515). M.D. was also supported by a NASA Future Investigators in NASA Earth and Space Science and Technology (FINESST) award (80NSSC24K1832). L.W. acknowledges funding by a Minghua Zhang Faculty Career Catalyst Award. The funders had no role in study design, data collection and analysis, decision to publish, or preparation of the manuscript.

bioRxiv preprint doi: https://doi.org/10.64898/2026.09.30.755482; this version posted October 18, 2026. The copyright holder for this preprint (which was not certified by peer review) is the author/funder, who has granted bioRxiv a license to display the preprint in perpetuity. It is made available under a CC-BY 4.0 International license.

Author contributions

M.D. designed the experiments, collected samples, performed laboratory experiments, analyzed and interpreted the data, prepared the figures, and wrote the manuscript. C.B. performed metagenomic analyses and contributed to data interpretation. A.H.F. performed nanoSIMS analyses and interpreted the data, with C.M.J.B. supervising nanoSIMS measurements. W.D.O. generated the total adenylate data. A.M.P. participated in shipboard sampling and laboratory work. Y.M. provided guidance on cell extraction methods. L.M.W. generated total organic carbon and δ^{13}Corg data. D.G. performed dissolved geochemical measurements. R.A.P. generated the bathymetric map. A.J.S., I.A., and T.W. participated in shipboard porewater sampling, including sample selection and preservation for post-cruise geochemical analyses. B.S., S.R.S., and J.S.-C. participated in shipboard sampling and sample processing. Y.Z. participated in shipboard sediment sampling and sample curation that contributed to the molecular datasets used in this study. E.A.S. participated in shipboard porewater sampling, including sample selection and preservation for post-cruise geochemical analyses. D.C.S. participated in shipboard operations and sample collection. A.E.D. supervised the nanoSIMS analyses. J.S.B. provided computational resources. All authors reviewed and edited the manuscript and approved the final version. D.H.B. and S.D. conceived and supervised the study and secured funding.

bioRxiv preprint doi: https://doi.org/10.64898/2026.09.30.755482; this version posted October 18, 2026. The copyright holder for this preprint (which was not certified by peer review) is the author/funder, who has granted bioRxiv a license to display the preprint in perpetuity. It is made available under a CC-BY 4.0 International license.

Competing interests

The authors declare no competing interests.

bioRxiv preprint doi: https://doi.org/10.64898/2026.09.30.755482; this version posted October 18, 2026. The copyright holder for this preprint (which was not certified by peer review) is the author/funder, who has granted bioRxiv a license to display the preprint in perpetuity. It is made available under a CC-BY 4.0 International license.

Data availability

The sequencing data generated in this study have been deposited in the NCBI Sequence Read Archive under BioProject accession PRJNA1541392. The data will be made publicly available upon publication and are available to reviewers upon request.

bioRxiv preprint doi: https://doi.org/10.64898/2026.09.30.755482; this version posted October 18, 2026. The copyright holder for this preprint (which was not certified by peer review) is the author/funder, who has granted bioRxiv a license to display the preprint in perpetuity. It is made available under a CC-BY 4.0 International license.

Code availability

Custom code used for bioinformatic and statistical analyses in this study is publicly available on GitHub at https://github.com/migdesmarais/Puerto-Rico-Trench-Piezophily.

bioRxiv preprint doi: https://doi.org/10.64898/2026.09.30.755482; this version posted October 18, 2026. The copyright holder for this preprint (which was not certified by peer review) is the author/funder, who has granted bioRxiv a license to display the preprint in perpetuity. It is made available under a CC-BY 4.0 International license.

Figure Legends

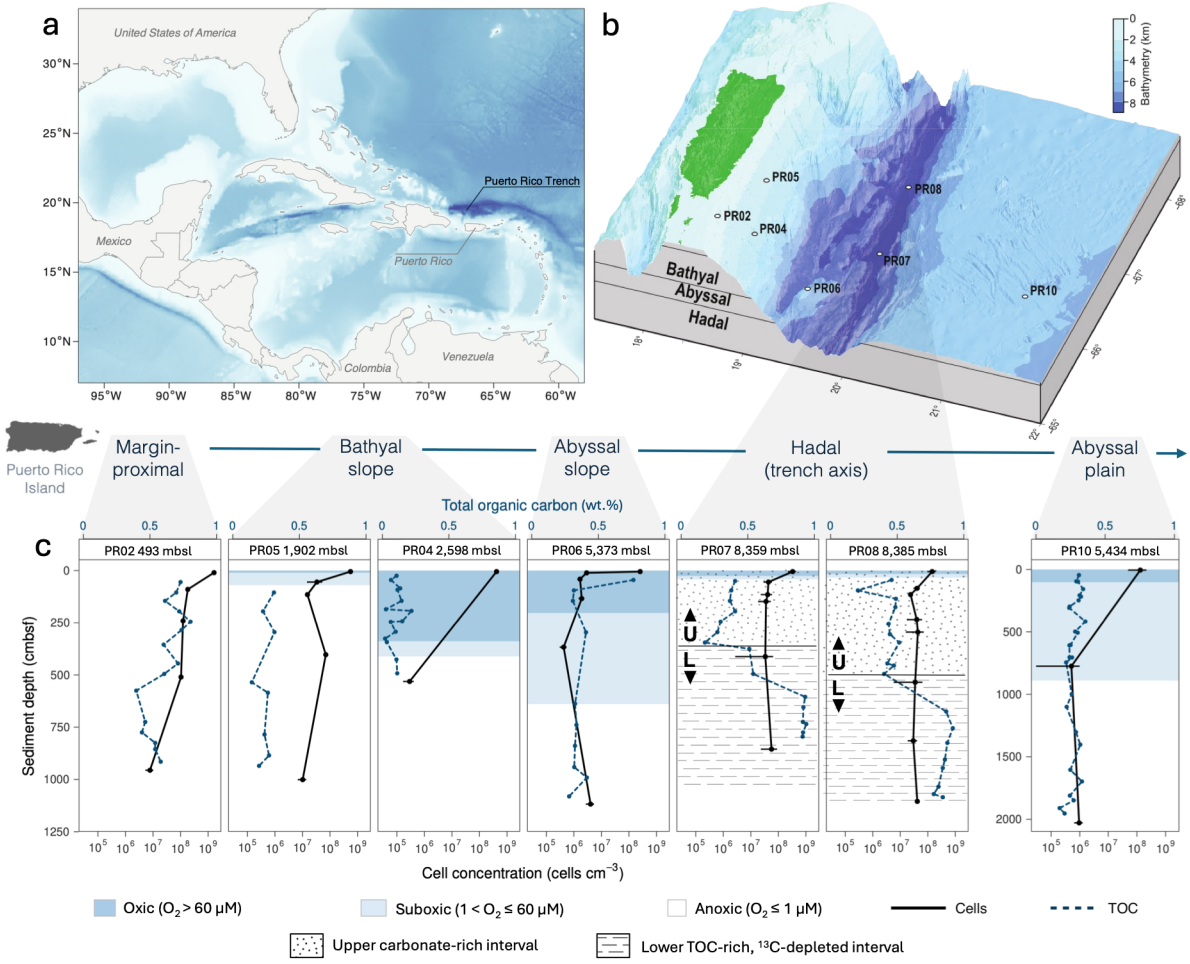
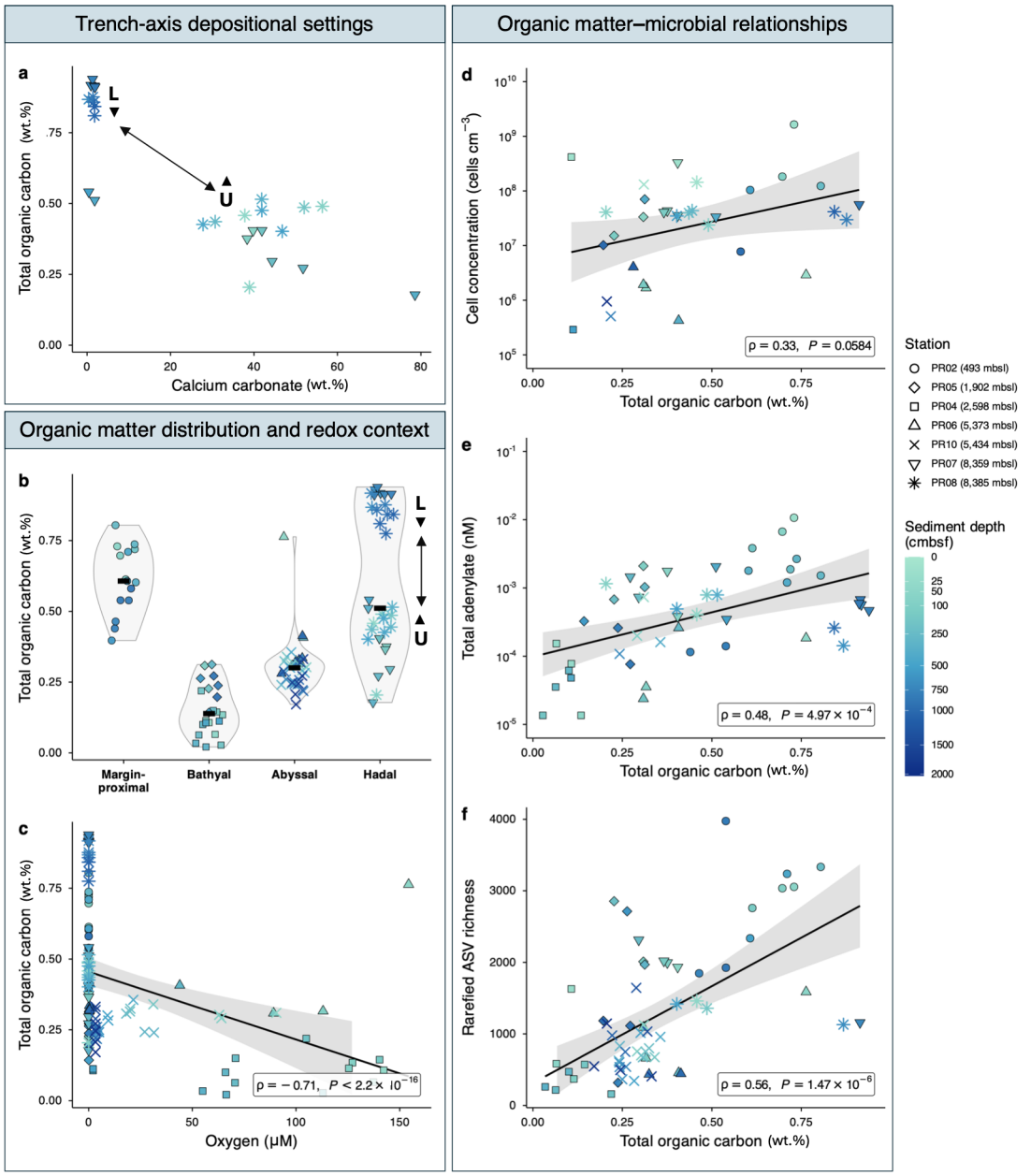


Fig. 1 | Organic matter, redox and microbial biomass vary across depositional settings, with pronounced heterogeneity at the trench axis. a, Regional location of the Puerto Rico Trench. b, Bathymetry and sampling sites. c, Sediment-depth profiles of cell concentration and total organic carbon content (TOC; wt.%) across redox zones and depositional intervals. Cell concentrations are shown as means of duplicate measurements; TOC content represents single measurements.

bioRxiv preprint doi: https://doi.org/10.64898/2026.09.30.755482; this version posted October 18, 2026. The copyright holder for this preprint (which was not certified by peer review) is the author/funder, who has granted bioRxiv a license to display the preprint in perpetuity. It is made available under a CC-BY 4.0 International license.



966

967 **Fig. 2 | Organic matter covaries with microbial biomass and diversity across the**

968 **transect but decouples in the lower trench-axis sediment interval. a,** Relationship

969 between total organic carbon (TOC; wt.%) and calcium carbonate ($CaCO_3$; wt.%) in

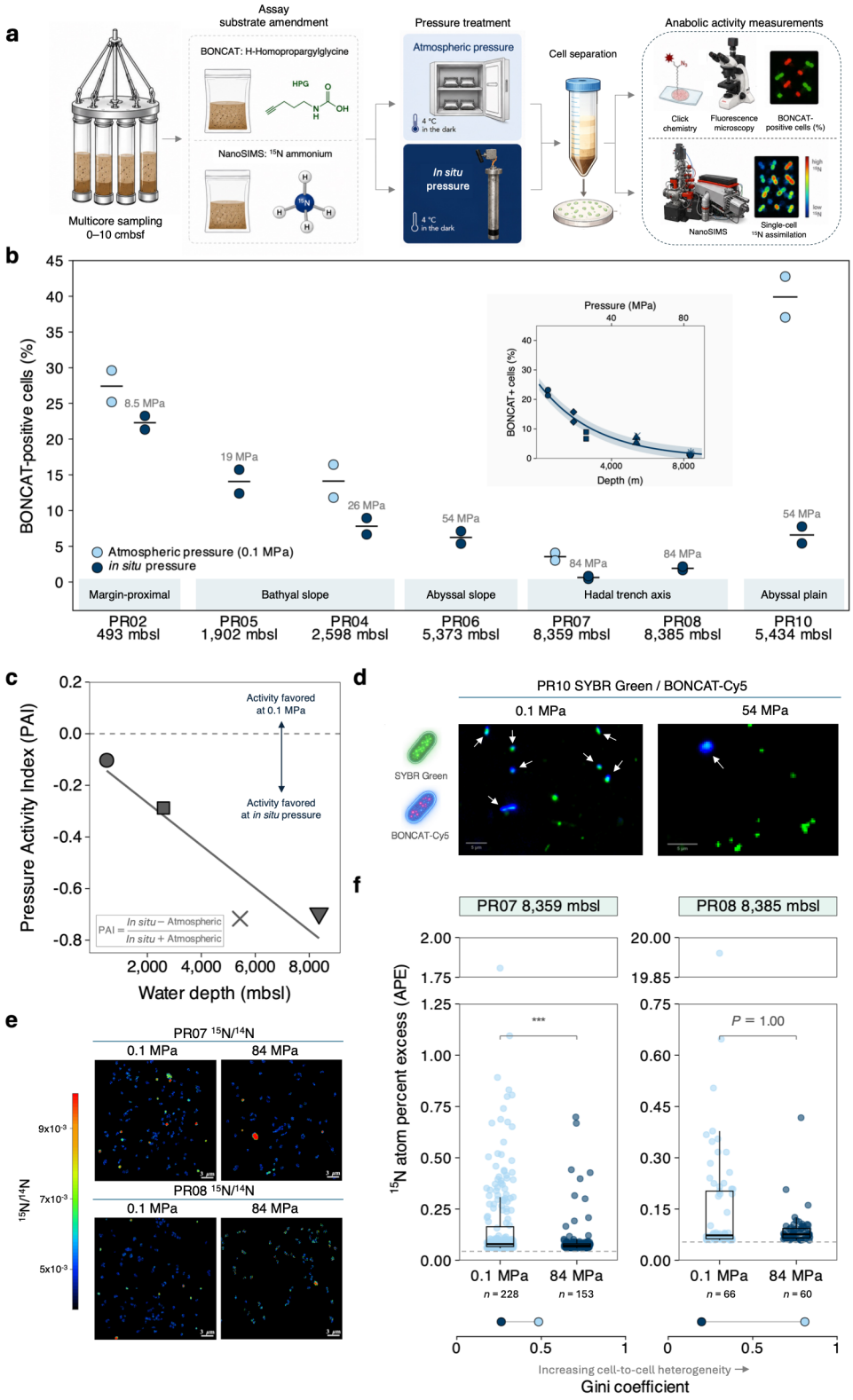
970 trench-axis sediments. **b,** TOC distributions across depositional settings. **c,** Relationship

971 between TOC and oxygen concentration (μM). **d–f,** Relationships between TOC and cell

bioRxiv preprint doi: https://doi.org/10.64898/2026.09.30.755482; this version posted October 18, 2026. The copyright holder for this preprint (which was not certified by peer review) is the author/funder, who has granted bioRxiv a license to display the preprint in perpetuity. It is made available under a CC-BY 4.0 International license.

concentration (cells cm^{-3}), total adenylate (ATP + ADP + AMP; nM) and rarefied amplicon sequence variant (ASV) richness, respectively. Black lines indicate linear regressions, with shading representing 95% confidence intervals; insets report Spearman ρ and *P* values. Correlation analyses include only samples with paired measurements.

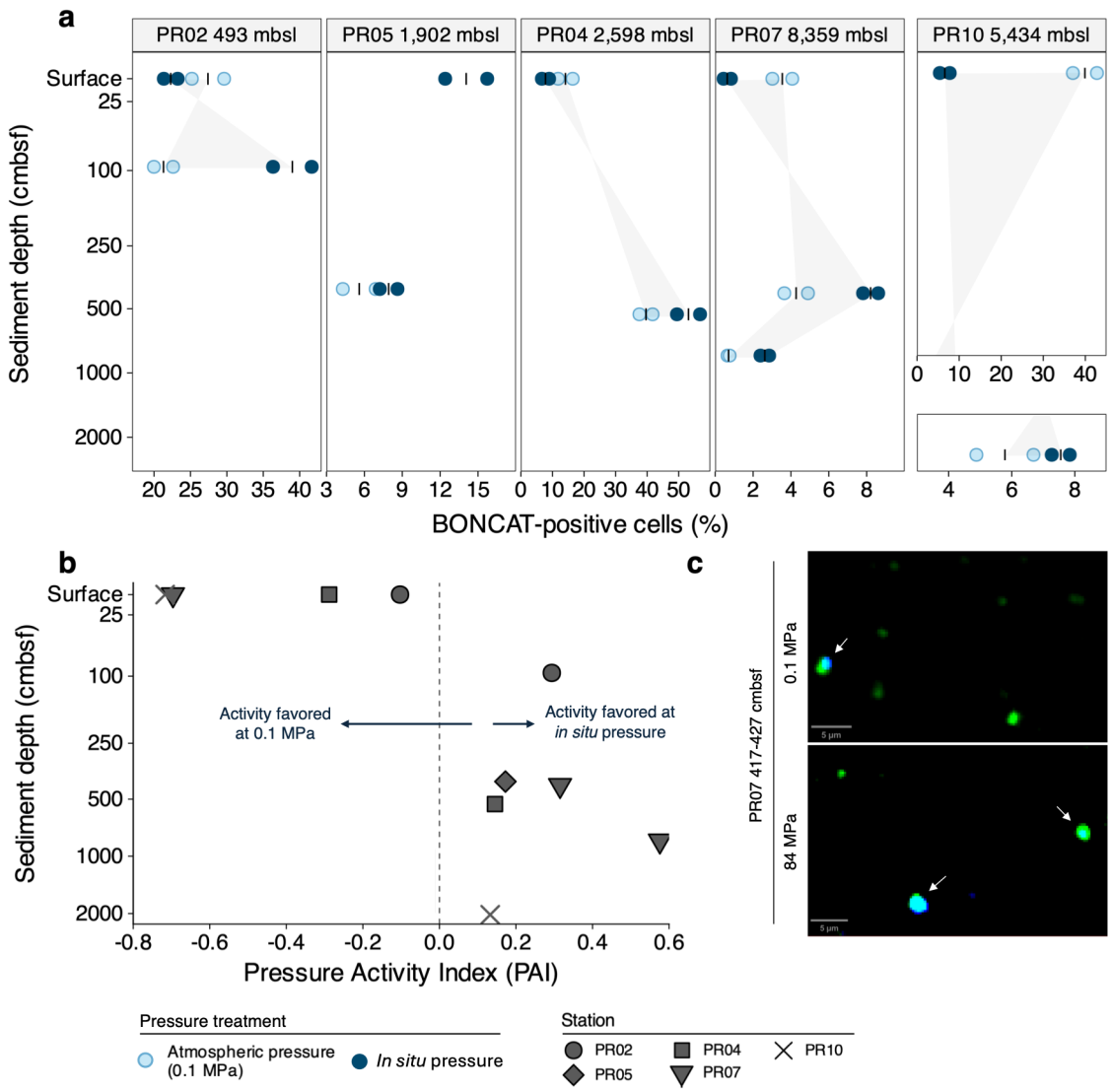
bioRxiv preprint doi: https://doi.org/10.64898/2026.09.30.755482; this version posted October 18, 2026. The copyright holder for this preprint (which was not certified by peer review) is the author/funder, who has granted bioRxiv a license to display the preprint in perpetuity. It is made available under a CC-BY 4.0 International license.



bioRxiv preprint doi: https://doi.org/10.64898/2026.09.30.755482; this version posted October 18, 2026. The copyright holder for this preprint (which was not certified by peer review) is the author/funder, who has granted bioRxiv a license to display the preprint in perpetuity. It is made available under a CC-BY 4.0 International license.

977 **Fig. 3 | Atmospheric pressure increases anabolic activity in surficial sediments. a,**
978 Workflow for paired atmospheric and *in situ* pressure incubations of surficial sediments
979 (0–10 cmbsf) followed by BONCAT and nanoSIMS. **b,** BONCAT-positive cells across
980 the transect (two independent incubation replicates per sample and pressure treatment);
981 inset shows the relationship between the *in situ*-pressure BONCAT-positive proportion
982 and water depth. **c,** Pressure Activity Index (PAI), calculated from the mean proportion of
983 BONCAT-positive cells for each pressure treatment; negative and positive values
984 indicate greater activity under atmospheric and *in situ* pressure, respectively. **d,**
985 Representative BONCAT fluorescence images from PR10; arrows indicate BONCAT-
986 positive cells. **e**, Representative nanoSIMS $^{15}N/^{14}N$ images from PR07 and PR08; areas
987 outside regions of interest (ROIs) interpreted as cells were set to zero and are shown in
988 black. **f**, Cellular ^{15}N atom percent excess (APE) among ^{15}N-active ROIs from PR07 and
989 PR08; dashed lines indicate the threshold used to classify ^{15}N-active ROIs. Boxes show
990 medians and interquartile ranges; *n* indicates ROIs analyzed. Each site and pressure
991 represents one incubation; statistical comparisons are based on cell-level distributions
992 rather than independent incubation replicates. Two-sided Wilcoxon rank-sum tests with
993 Bonferroni correction (***$P < 0.001$; PR08, adjusted $P = 1.00$). Gini coefficients indicate
994 cell-to-cell heterogeneity in ^{15}N assimilation.

bioRxiv preprint doi: https://doi.org/10.64898/2026.09.30.755482; this version posted October 18, 2026. The copyright holder for this preprint (which was not certified by peer review) is the author/funder, who has granted bioRxiv a license to display the preprint in perpetuity. It is made available under a CC-BY 4.0 International license.



995

996 **Fig. 4 | Microbial pressure responses reverse with burial from atmospheric-**

997 **pressure-favored to *in situ*-pressure-favored activity. a,** BONCAT-positive cells in

998 surface and subsurface sediments under atmospheric and *in situ* pressure (two

999 independent incubations per sample and pressure treatment). Grey shaded areas connect

1000 atmospheric- and *in situ*-pressure treatment means across sediment depths, highlighting

1001 the reversal in pressure response with burial. **b,** Pressure Activity Index (PAI) across

1002 sediment depths, calculated from the mean proportion of BONCAT-positive cells for

bioRxiv preprint doi: https://doi.org/10.64898/2026.09.30.755482; this version posted October 18, 2026. The copyright holder for this preprint (which was not certified by peer review) is the author/funder, who has granted bioRxiv a license to display the preprint in perpetuity. It is made available under a CC-BY 4.0 International license.

each pressure treatment; negative and positive values indicate greater activity under atmospheric and *in situ* pressure, respectively. **c,** Representative BONCAT fluorescence images from PR07 at 417–427 cmbsf under atmospheric and *in situ* pressure; arrows indicate BONCAT-positive cells.

bioRxiv preprint doi: https://doi.org/10.64898/2026.09.30.755482; this version posted October 18, 2026. The copyright holder for this preprint (which was not certified by peer review) is the author/funder, who has granted bioRxiv a license to display the preprint in perpetuity. It is made available under a CC-BY 4.0 International license.

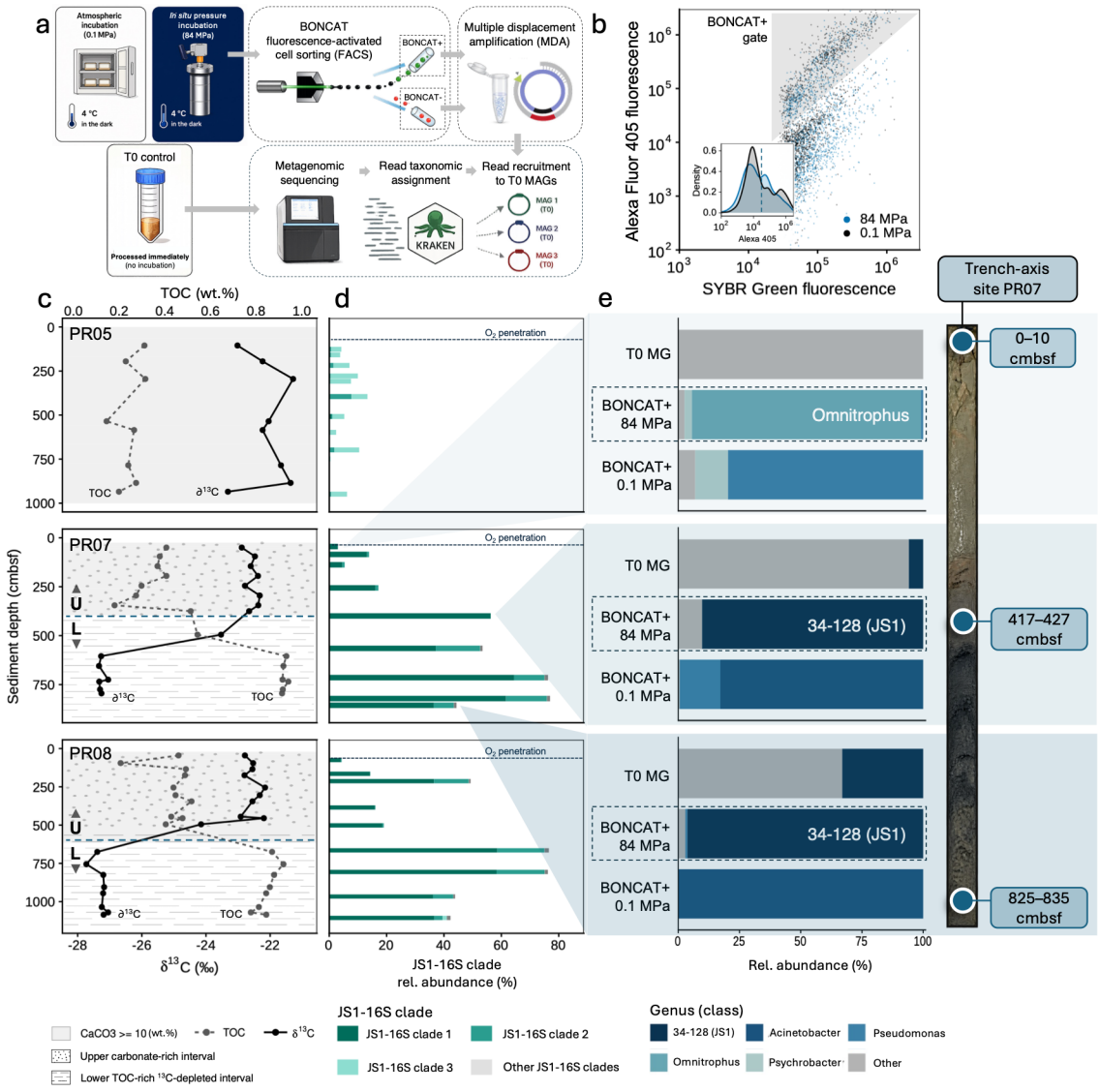


Fig. 5 | Abundant trench-axis JS1 populations are associated with distinct depositional intervals and anabolic activity under *in situ* pressure. a, BONCAT-FACS-seq workflow for atmospheric and *in situ* pressure incubations and T_0 metagenomic controls. **b,** Representative BONCAT-positive FACS gate and Alexa Fluor 405 fluorescence distributions. **c,** Total organic carbon (TOC; wt.%) and $\delta^{13}C_{org}$ (‰) profiles across depositional intervals at PR05, PR07 and PR08. **d,** Relative abundance of JS1 16S rRNA gene clades with sediment depth. **e,** Genus-level composition of T_0

bioRxiv preprint doi: https://doi.org/10.64898/2026.09.30.755482; this version posted October 18, 2026. The copyright holder for this preprint (which was not certified by peer review) is the author/funder, who has granted bioRxiv a license to display the preprint in perpetuity. It is made available under a CC-BY 4.0 International license.

metagenomes and BONCAT-positive fractions under atmospheric and *in situ* pressure at trench-axis site PR07.

bioRxiv preprint doi: https://doi.org/10.64898/2026.09.30.755482; this version posted October 18, 2026. The copyright holder for this preprint (which was not certified by peer review) is the author/funder, who has granted bioRxiv a license to display the preprint in perpetuity. It is made available under a CC-BY 4.0 International license.

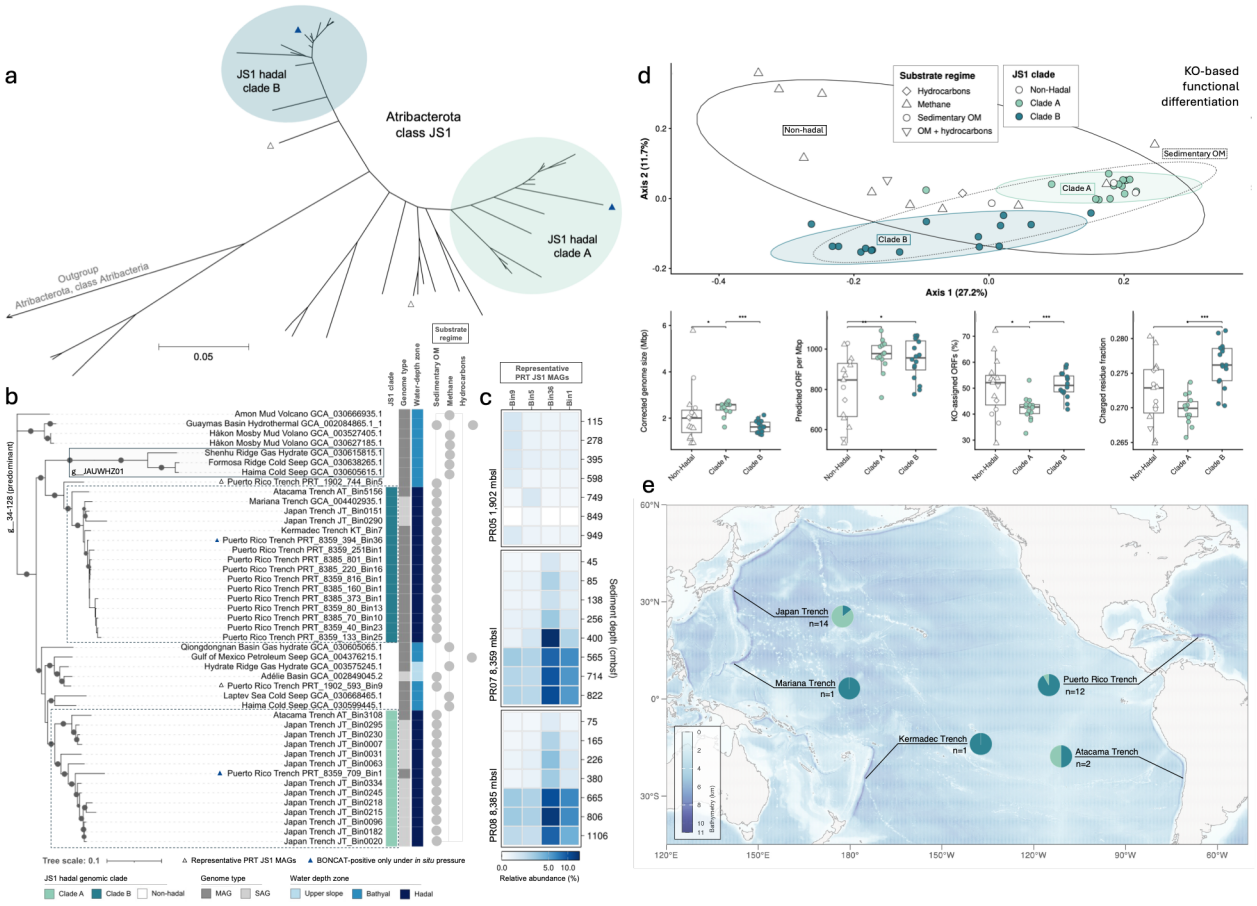


Fig. 6 | *In situ*-pressure-active JS1 populations belong to genomically differentiated clades widespread across hadal trenches. a, Simplified phylogenomic topology of JS1, highlighting hadal clades A and B. **b,** Detailed maximum-likelihood JS1 phylogeny annotated by JS1 clade, genome type, water-depth zone and substrate regime. Node size represents ultrafast bootstrap support based on 1,000 replicates. Filled blue triangles indicate Puerto Rico Trench MAGs detected in BONCAT-positive fractions under *in situ* but not atmospheric pressure. **c,** Relative abundance of representative PRT JS1 MAGs across sediment depths at PR05, PR07 and PR08. **d,** KEGG Ortholog (KO)-based functional differentiation and genome properties among non-hadal JS1 (n = 15 genomes), hadal clade A (n = 14) and hadal clade B (n = 16). The principal coordinates analysis

bioRxiv preprint doi: https://doi.org/10.64898/2026.09.30.755482; this version posted October 18, 2026. The copyright holder for this preprint (which was not certified by peer review) is the author/funder, who has granted bioRxiv a license to display the preprint in perpetuity. It is made available under a CC-BY 4.0 International license.

(PCoA) shows Bray–Curtis dissimilarities of KO profiles. KO-profile differences were assessed by PERMANOVA; boxes show medians and interquartile ranges, with asterisks indicating pairwise Wilcoxon rank-sum tests with Benjamini–Hochberg-adjusted *P* values (*$P < 0.05$, **$P < 0.01$, ***$P < 0.001$). **e,** Geographic distribution and number of publicly available JS1 MAGs assigned to hadal clades A and B across five hadal trenches.

bioRxiv preprint doi: https://doi.org/10.64898/2026.09.30.755482; this version posted October 18, 2026. The copyright holder for this preprint (which was not certified by peer review) is the author/funder, who has granted bioRxiv a license to display the preprint in perpetuity. It is made available under a CC-BY 4.0 International license.

Extended Data Figure Legends

Extended Data Fig. 1 | Geochemical, redox, biomass-linked and diversity profiles across the Puerto Rico Trench transect. a,b, δ^{13}Corg (‰) and calcium carbonate (CaCO3; wt.%) profiles. c,d, Oxygen (μM), nitrate (μM kg^{-1}) and sulfate (mM kg^{-1}) profiles. e, Total adenylate concentration (ATP + ADP + AMP; nM). f, Estimated adenylate content per cell (nmol $cell^{-1}$). g, Rarefied amplicon sequence variant (ASV) richness. Dashed lines mark the boundary between the upper carbonate-rich (U) and lower TOC-rich, ^{13}C-depleted (L) intervals at PR07 and PR08.

Extended Data Fig. 2 | Lithological transition in PR07 trench-axis sediments. Split-core images showing the transition from the lighter-colored upper carbonate-rich interval (U) to the darker-colored lower TOC-rich, ^{13}C-depleted interval (L). The boundary between intervals occurs at approximately 425 cmbsf.

Extended Data Fig. 3 | Relationships among organic matter properties and microbial proxies across the Puerto Rico Trench transect. a–c, Relationships of total nitrogen content (TN; wt.%) with cell concentration (cells cm^{-3}), total adenylate (ATP + ADP + AMP; nM) and rarefied amplicon sequence variant (ASV) richness, respectively. **d–f,** Pairwise relationships among these microbial proxies. **g–i,** Distributions of each proxy across depositional settings. **j–l,** Relationships of $\delta^{13}C_{org}$ (‰) with cell concentration, total adenylate and rarefied ASV richness, respectively. Black lines and shading show fitted relationships and 95% confidence intervals. Insets report Spearman ρ and *P* values.

bioRxiv preprint doi: https://doi.org/10.64898/2026.09.30.755482; this version posted October 18, 2026. The copyright holder for this preprint (which was not certified by peer review) is the author/funder, who has granted bioRxiv a license to display the preprint in perpetuity. It is made available under a CC-BY 4.0 International license.

Extended Data Fig. 4 | BONCAT-FACS gating and taxonomic composition of sorted PR07 sediment communities. a, Sequential FACS gating of parent cells (P1), BONCAT-positive cells (P2) and below-threshold (B-T) cells (P3). **b,** SYBR Green and Alexa Fluor 405 fluorescence during sorting of PR07 sediments at 0–10, 417–427 and 825–835 cmbsf incubated under atmospheric and *in situ* pressure; shading indicates the BONCAT-positive gate, and insets show Alexa Fluor 405 distributions. **c,** HPG-amended copper-omission control used to define the BONCAT-positive fluorescence threshold and reagent-only PBS control. **d,** Class-level taxonomic composition of T_0 metagenomes and BONCAT-positive and below-threshold sorted fractions across sediment depths and pressure treatments.

Extended Data Fig. 5 | Composition and genome properties of the JS1 genome collection. a, MAG and SAG composition among non-hadal JS1 and hadal clades A and B. **b,** Trench and source composition of each genomic group. **c–e,** CheckM completeness (%), contamination (%) and GC content (%), respectively. Points represent individual genomes; boxes show medians and interquartile ranges.

Extended Data Fig. 6 | Pairwise average amino acid identity among JS1 genomes. Heatmap of pairwise average amino acid identity (AAI), with colors indicating genus-level (65–95% AAI) and species-level (≥95% AAI) ranges. Boxes delineate hadal clades A and B.

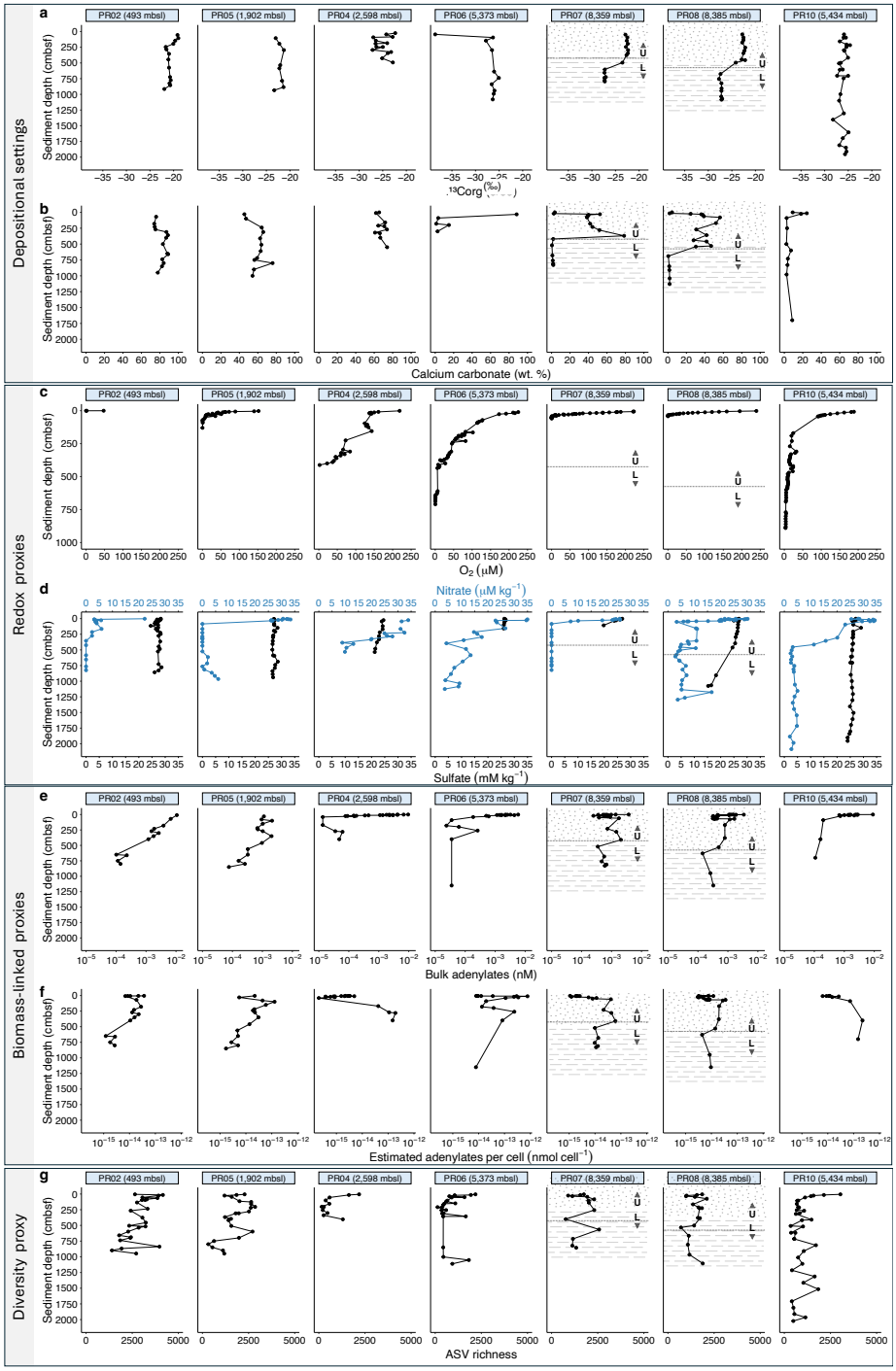
Extended Data Fig. 7 | Proteome physicochemical properties across JS1 genomic groups. a, Median protein isoelectric point (pI). **b,** Acidic-to-basic residue ratio. **c,** Charged-residue fraction. **d,** Hydrophobic-residue fraction. Points represent individual

bioRxiv preprint doi: https://doi.org/10.64898/2026.09.30.755482; this version posted October 18, 2026. The copyright holder for this preprint (which was not certified by peer review) is the author/funder, who has granted bioRxiv a license to display the preprint in perpetuity. It is made available under a CC-BY 4.0 International license.

genomes; boxes show medians and interquartile ranges. Pairwise Wilcoxon rank-sum tests with Benjamini–Hochberg-adjusted *P* values (*$P < 0.05$, **$P < 0.01$, ***$P < 0.001$).

bioRxiv preprint doi: https://doi.org/10.64898/2026.09.30.755482; this version posted October 18, 2026. The copyright holder for this preprint (which was not certified by peer review) is the author/funder, who has granted bioRxiv a license to display the preprint in perpetuity. It is made available under a CC-BY 4.0 International license.

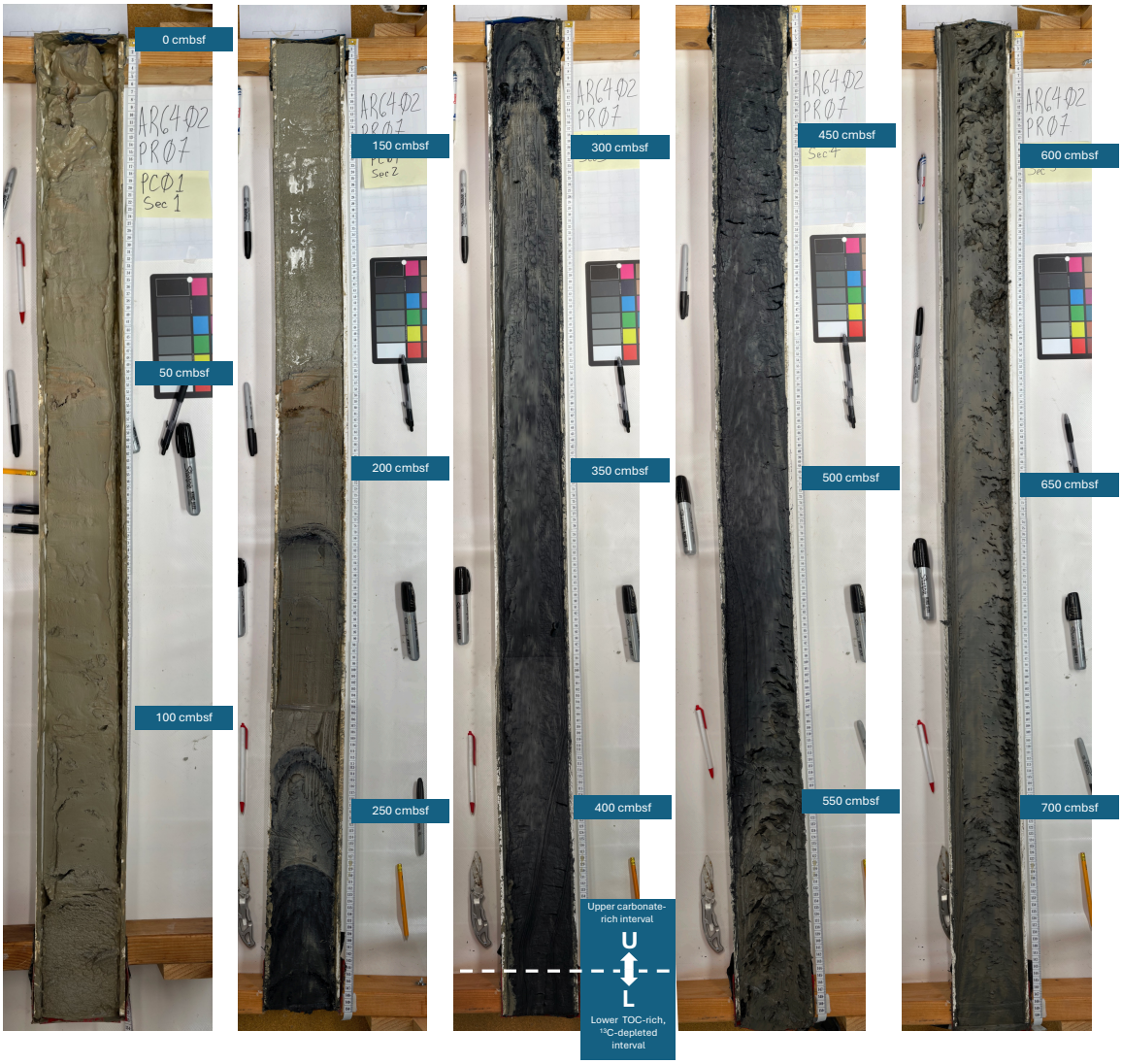
Extended Data Figures



Extended Data Fig. 1 | Geochemical, redox, biomass-linked and diversity profiles across the Puerto Rico Trench transect. a,b, δ^{13}Corg (‰) and calcium carbonate

bioRxiv preprint doi: https://doi.org/10.64898/2026.09.30.755482; this version posted October 18, 2026. The copyright holder for this preprint (which was not certified by peer review) is the author/funder, who has granted bioRxiv a license to display the preprint in perpetuity. It is made available under a CC-BY 4.0 International license.

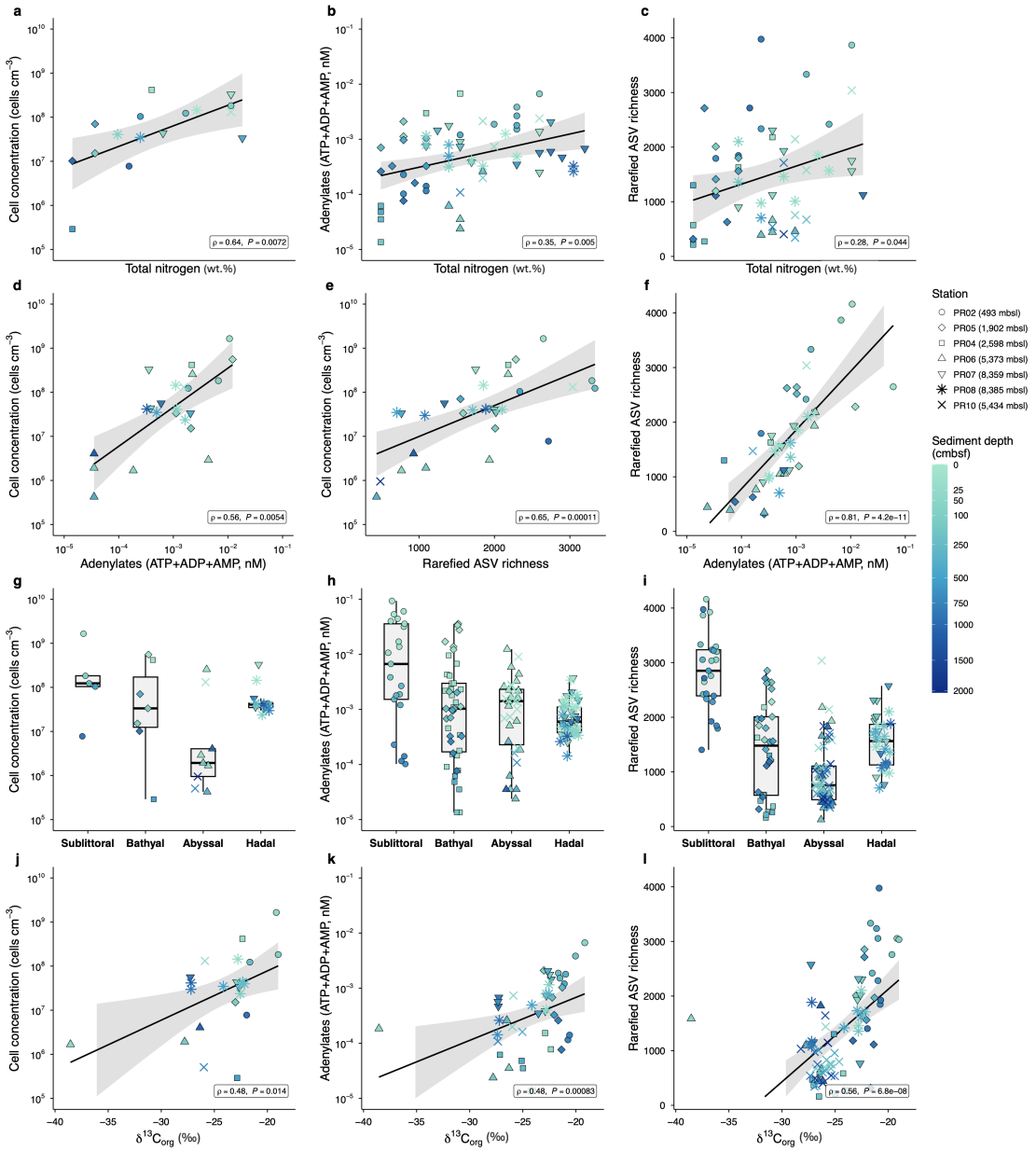
(CaCO3; wt.%) profiles. c,d, Oxygen (μM), nitrate (μM kg^{-1}) and sulfate (mM kg^{-1}) profiles. e, Total adenylate concentration (ATP + ADP + AMP; nM). f, Estimated adenylate content per cell (nmol $cell^{-1}$). g, Rarefied amplicon sequence variant (ASV) richness. Dashed lines mark the boundary between the upper carbonate-rich (U) and lower TOC-rich, ^{13}C-depleted (L) intervals at PR07 and PR08.



11

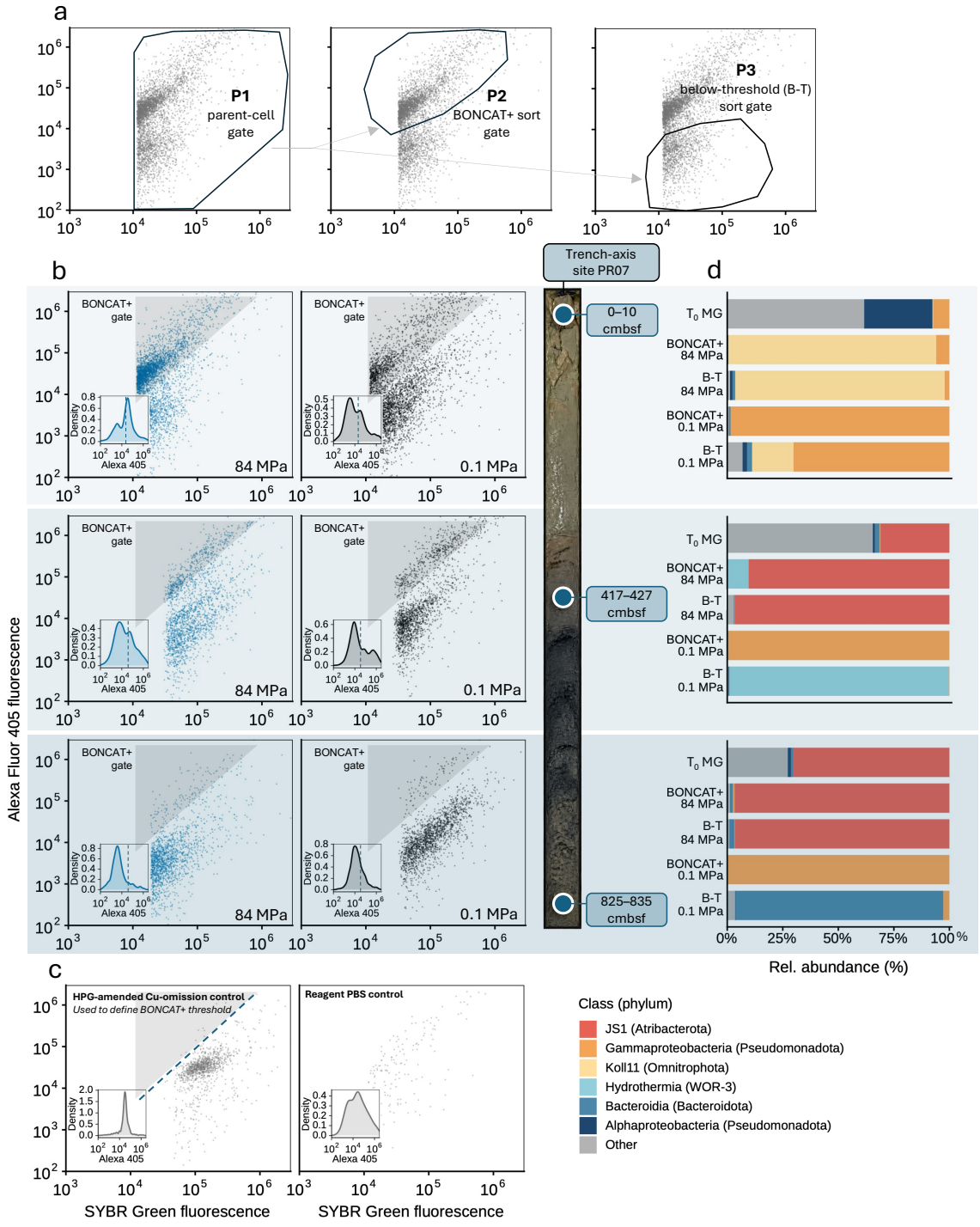
12 **Extended Data Fig. 2 | Lithological transition in PR07 trench-axis sediments.** Split-
13 core images showing the transition from the lighter-colored upper carbonate-rich interval
14 (U) to the darker-colored lower TOC-rich, ^{13}C-depleted interval (L). The boundary
15 between intervals occurs at approximately 425 cmbsf.

16



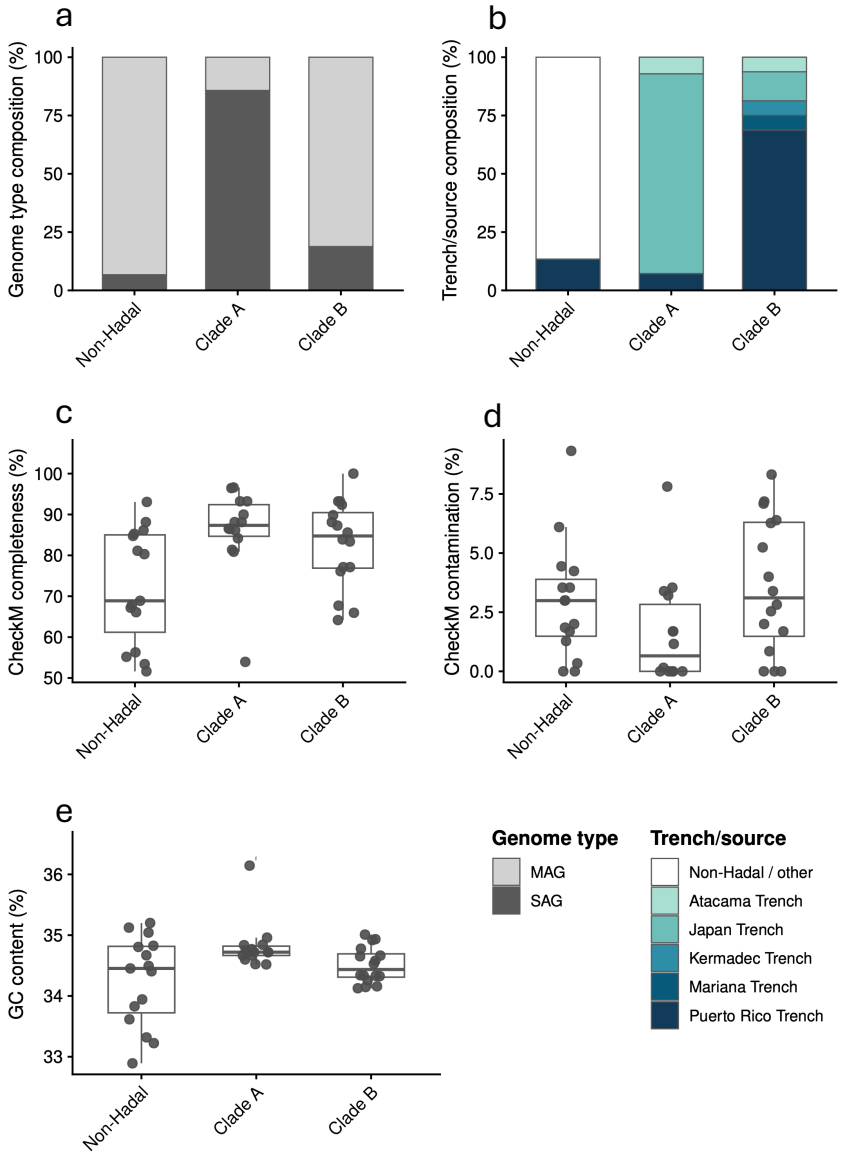
Extended Data Fig. 3 | Relationships among organic matter properties and microbial proxies across the Puerto Rico Trench transect. a–c, Relationships of total nitrogen content (TN; wt.%) with cell concentration (cells cm^{-3}), total adenylate (ATP + ADP + AMP; nM) and rarefied amplicon sequence variant (ASV) richness, respectively. **d–f,** Pairwise relationships among these microbial proxies. **g–i,** Distributions of each

proxy across depositional settings. **j–l,** Relationships of $\delta^{13}C_{org}$ (‰) with cell concentration, total adenylate and rarefied ASV richness, respectively. Black lines and shading show fitted relationships and 95% confidence intervals. Insets report Spearman ρ and *P* values.



Extended Data Fig. 4 | BONCAT-FACS gating and taxonomic composition of sorted PR07 sediment communities. a, Sequential FACS gating of parent cells (P1), BONCAT-positive cells (P2) and below-threshold (B-T) cells (P3). **b,** SYBR Green and

Alexa Fluor 405 fluorescence during sorting of PR07 sediments at 0–10, 417–427 and 825–835 cmbsf incubated under atmospheric and *in situ* pressure; shading indicates the BONCAT-positive gate, and insets show Alexa Fluor 405 distributions. **c,** HPG-amended copper-omission control used to define the BONCAT-positive fluorescence threshold and reagent-only PBS control. **d,** Class-level taxonomic composition of T_0 metagenomes and BONCAT-positive and below-threshold sorted fractions across sediment depths and pressure treatments.



39

40 **Extended Data Fig. 5 | Composition and genome properties of the JS1 genome**

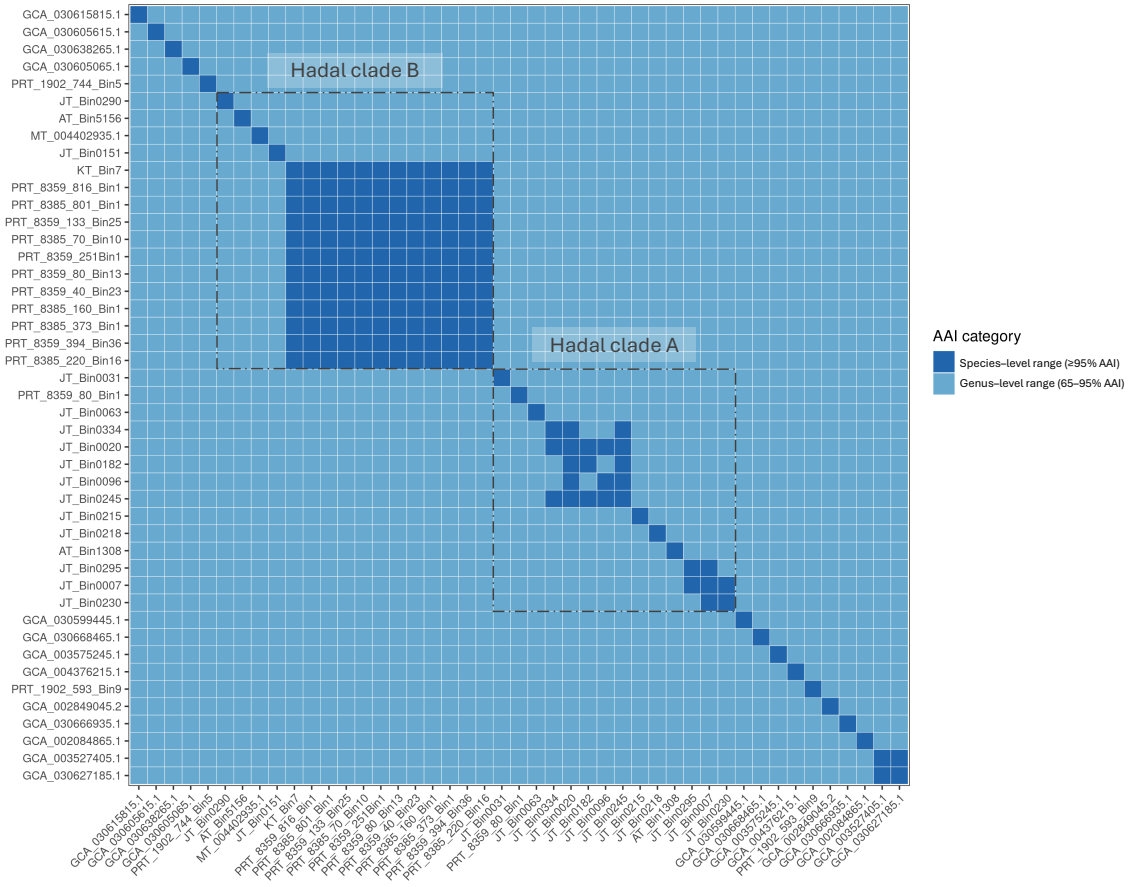
41 **collection. a,** MAG and SAG composition among non-hadal JS1 and hadal clades A and

42 B. **b,** Trench and source composition of each genomic group. **c–e,** CheckM completeness

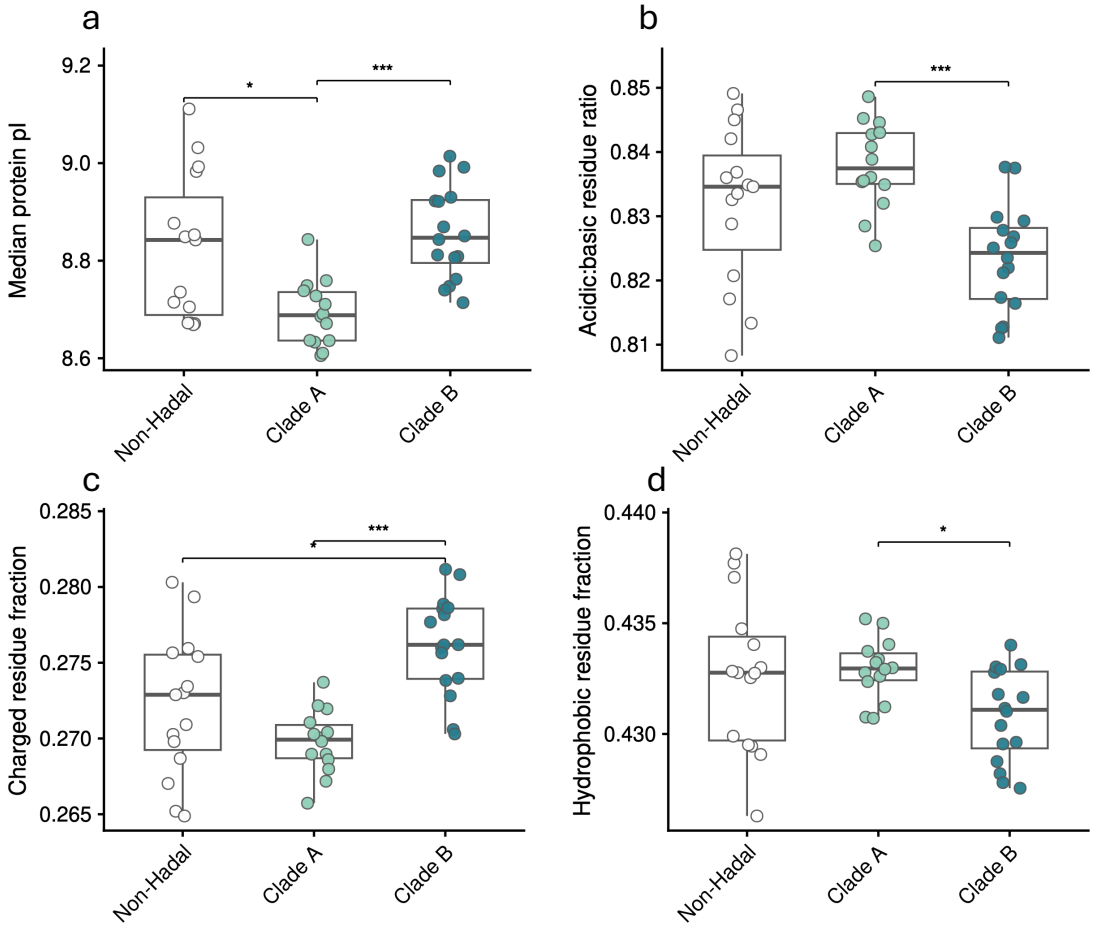
43 (%), contamination (%) and GC content (%), respectively. Points represent individual

44 genomes; boxes show medians and interquartile ranges.

45



Extended Data Fig. 6 | Pairwise average amino acid identity among JS1 genomes. Heatmap of pairwise average amino acid identity (AAI), with colors indicating genus-level (65–95% AAI) and species-level (≥95% AAI) ranges. Boxes delineate hadal clades A and B.



52

53 **Extended Data Fig. 7 | Proteome physicochemical properties across JS1 genomic**

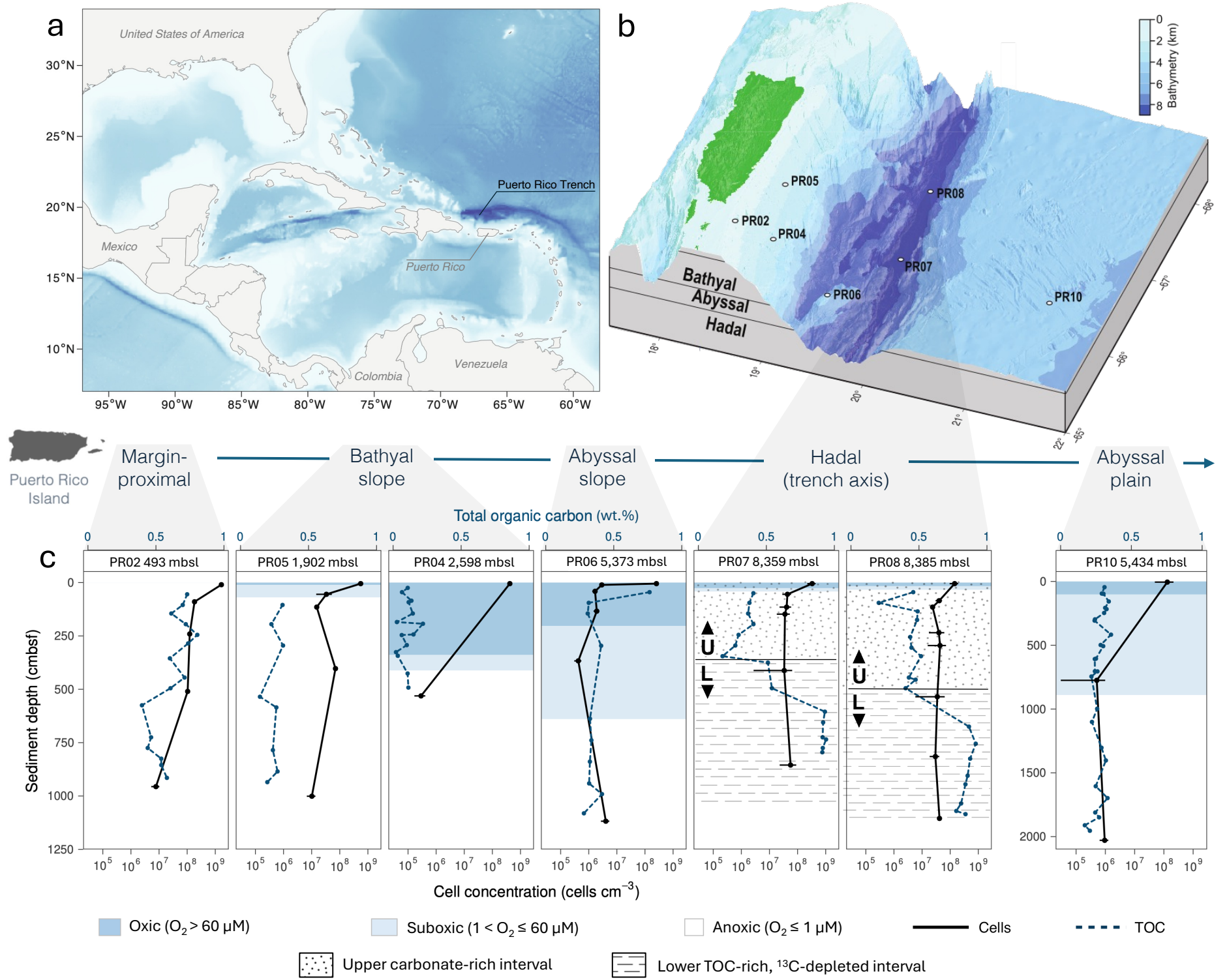
54 **groups. a,** Median protein isoelectric point (pI). **b,** Acidic-to-basic residue ratio. **c,**

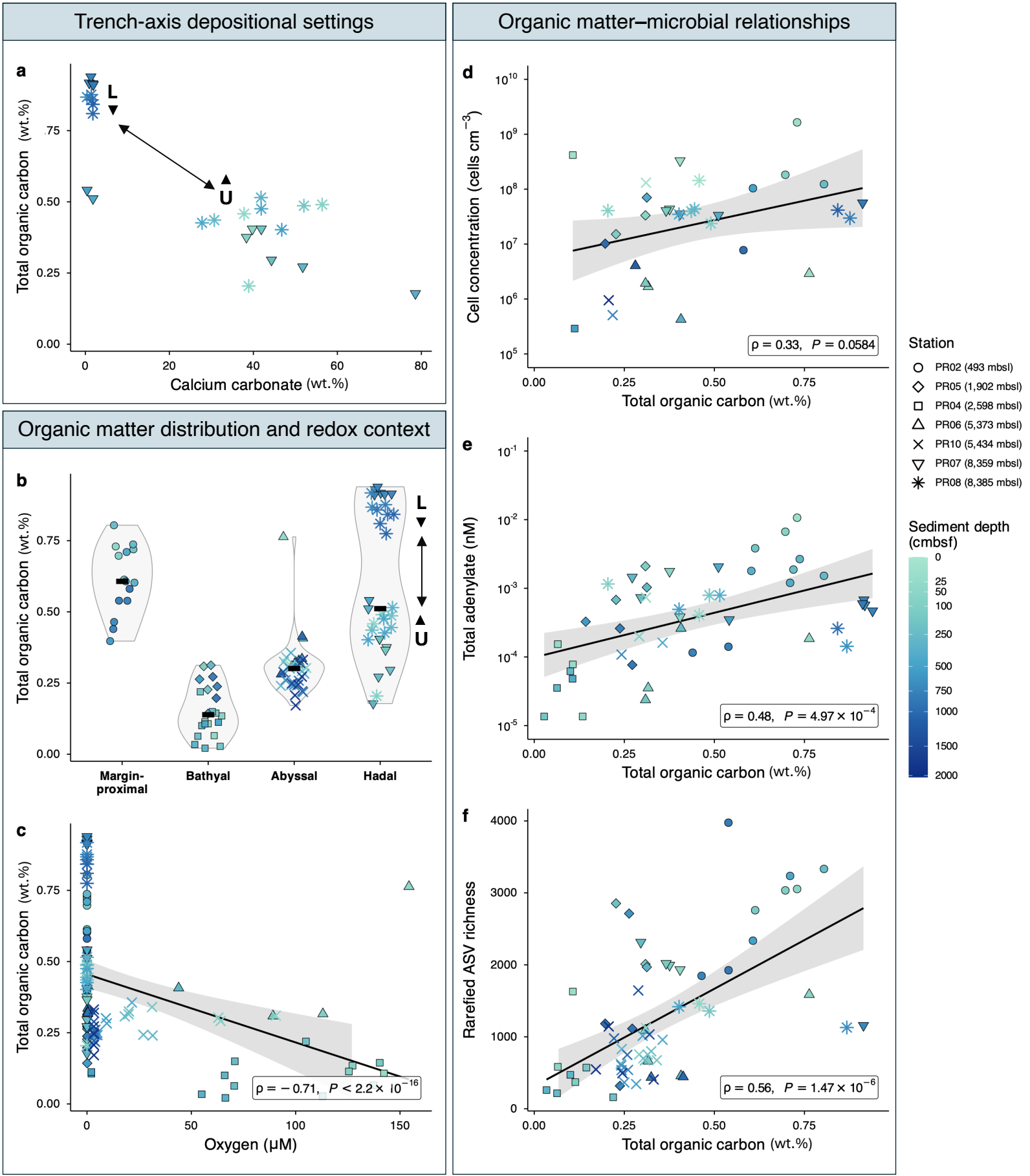
55 Charged-residue fraction. **d,** Hydrophobic-residue fraction. Points represent individual

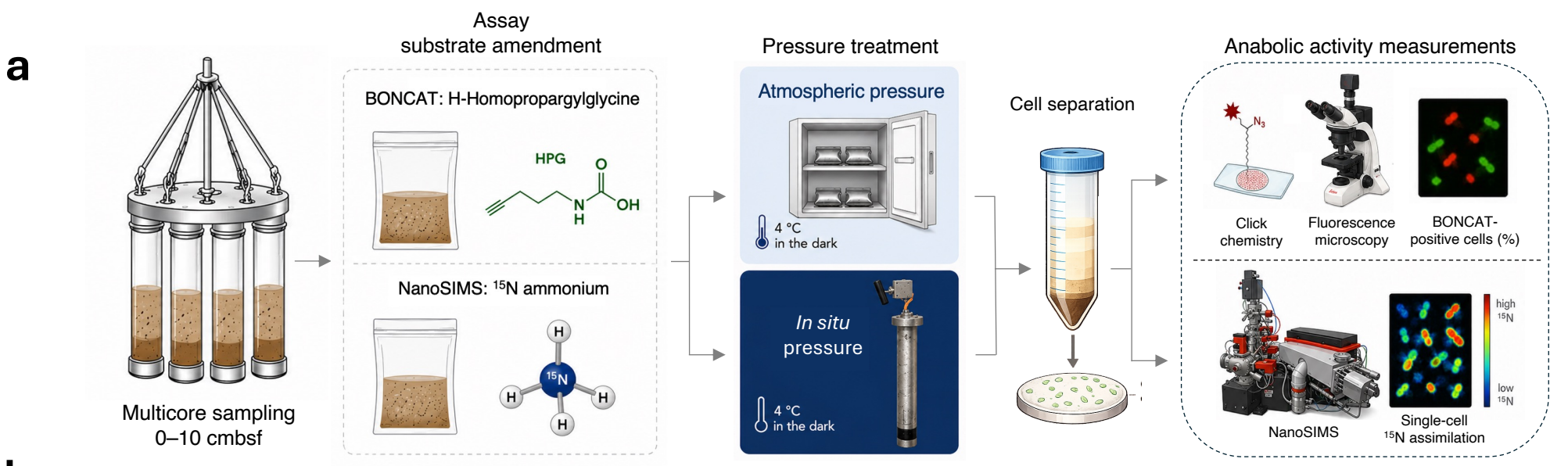
56 genomes; boxes show medians and interquartile ranges. Pairwise Wilcoxon rank-sum

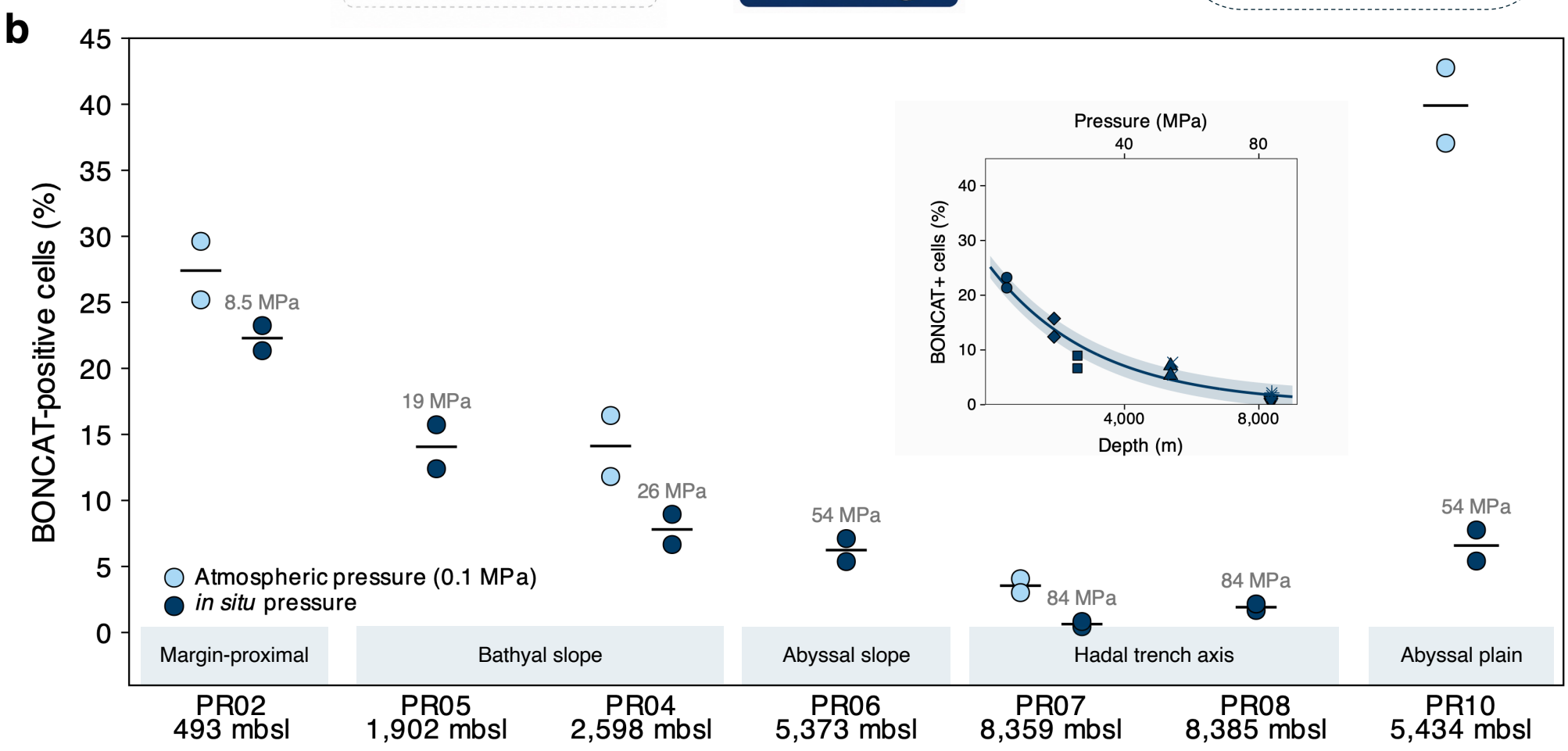
57 tests with Benjamini–Hochberg-adjusted *P* values (*$P < 0.05$, **$P < 0.01$, ***$P < 0.001$).

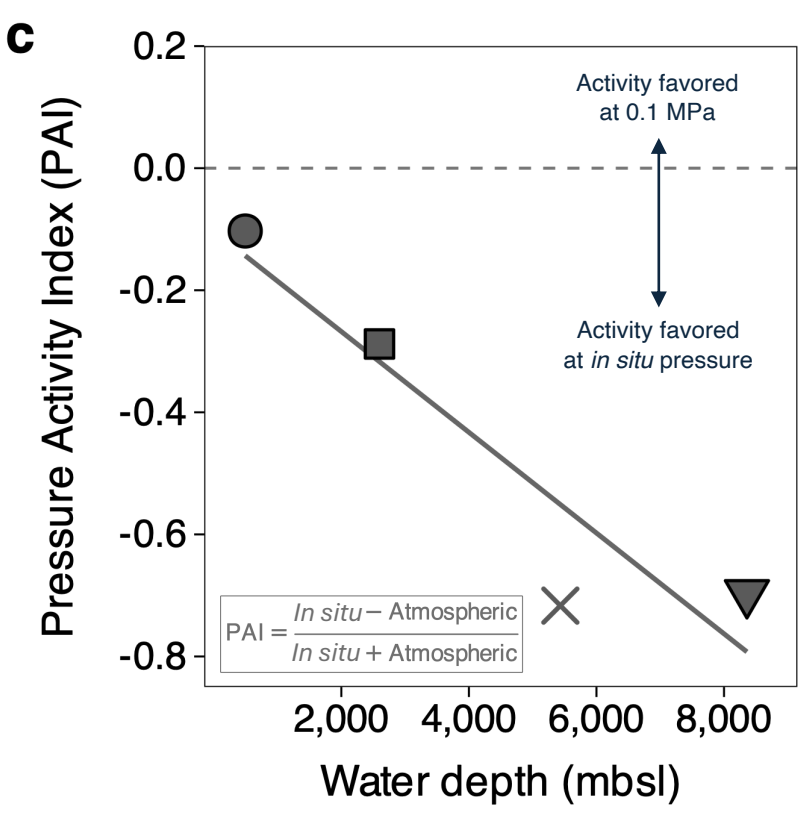
58

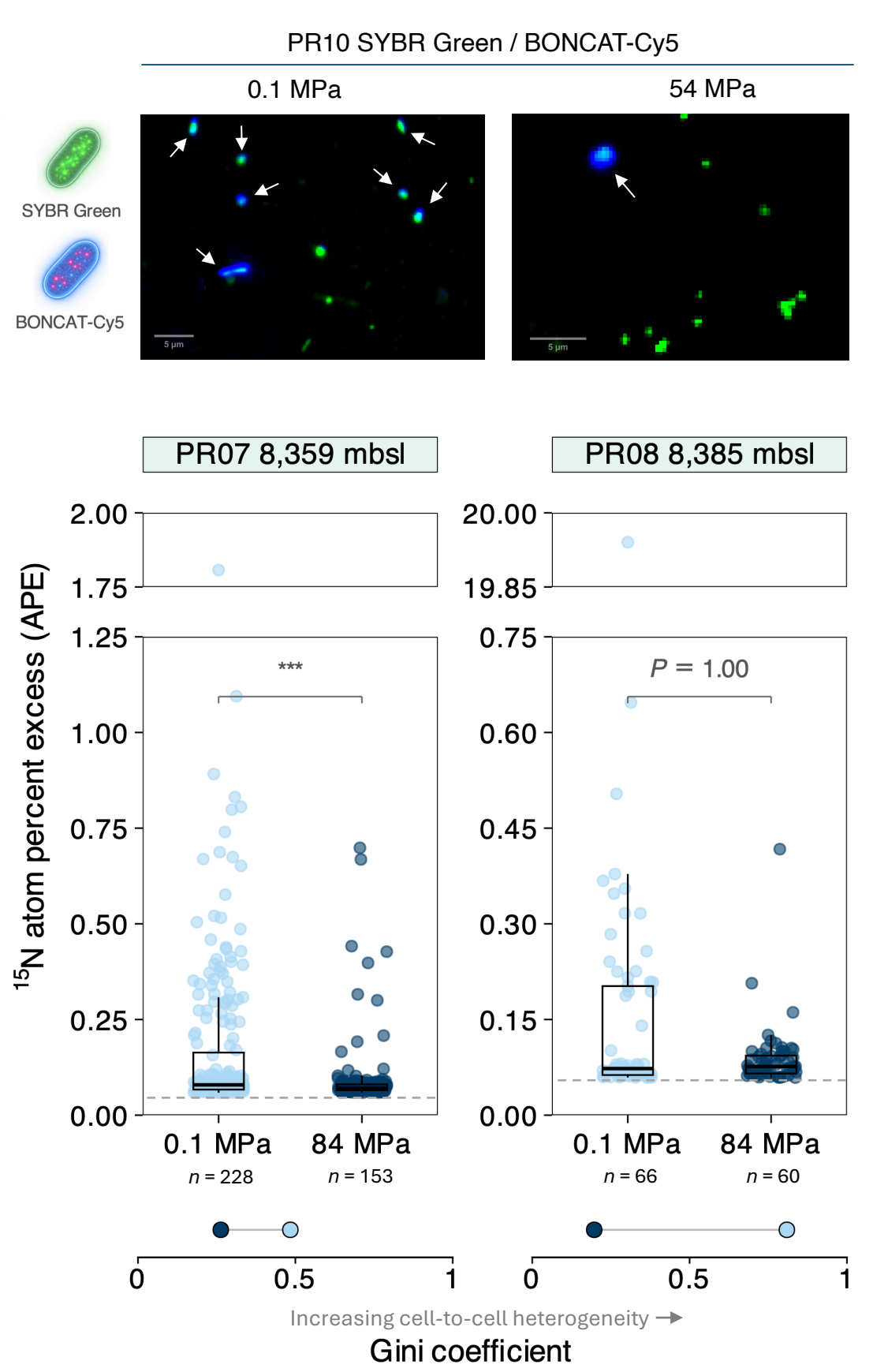

a
United States of America
Mexico
Puerto Rico
Venezuela
Colombia
Puerto Rico Trench
30°N
25°N
20°N
15°N
10°N
95°W
90°W
85°W
80°W
75°W
70°W
65°W
60°W
b
Bathymetry (km)
0
2
4
6
8
PR05
PR08
PR02
PR04
PR07
PR06
PR10
Bathyal
Abyssal
Hadal
Puerto Rico Island
Margin-proximal
Bathyal slope
Abyssal slope
Hadal (trench axis)
Abyssal plain
Total organic carbon (wt.%)
c
PR02 493 mbsl
PR05 1,902 mbsl
PR04 2,598 mbsl
PR06 5,373 mbsl
PR07 8,359 mbsl
PR08 8,385 mbsl
PR10 5,434 mbsl
U
L
Sediment depth (cmbsf)
Cell concentration (cells cm−3)
Oxic (O2 > 60 µM)
Suboxic (1 < O2 ≤ 60 µM)
Anoxic (O2 ≤ 1 µM)
Cells
TOC
Upper carbonate-rich interval
Lower TOC-rich, 13C-depleted interval

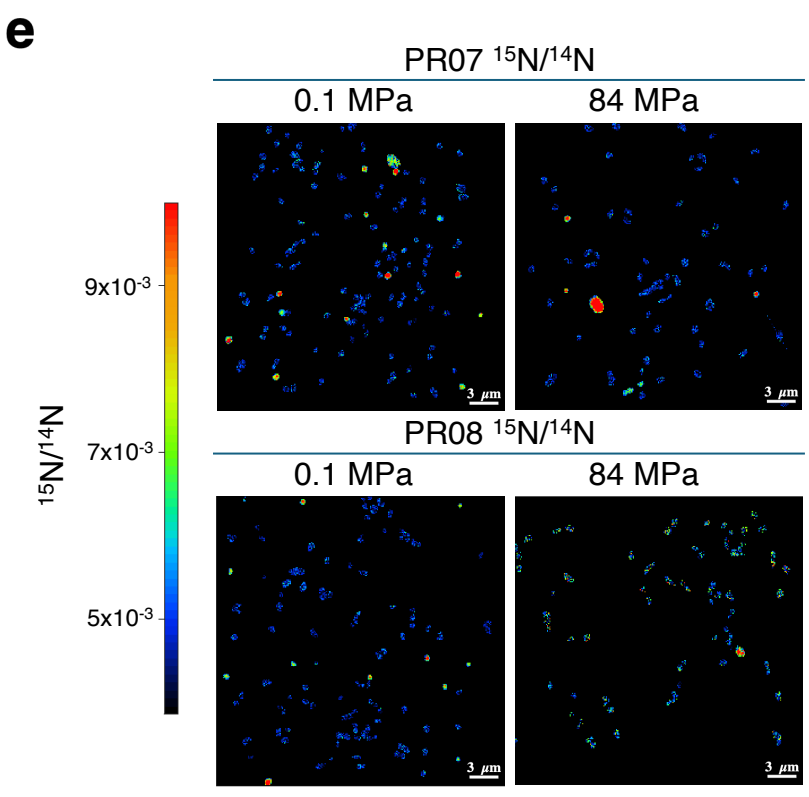

Trench-axis depositional settings
Organic matter distribution and redox context
Organic matter–microbial relationships
a
L
U
Total organic carbon (wt.%)
Calcium carbonate (wt.%)
b
Total organic carbon (wt.%)
Margin-proximal
Bathyal
Abyssal
Hadal
c
Total organic carbon (wt.%)
ρ = −0.71, P < 2.2 × 10−16
Oxygen (μM)
d
Cell concentration (cells cm−3)
ρ = 0.33, P = 0.0584
Total organic carbon (wt.%)
e
Total adenylate (nM)
ρ = 0.48, P = 4.97 × 10−4
Total organic carbon (wt.%)
f
Rarefied ASV richness
ρ = 0.56, P = 1.47 × 10−6
Total organic carbon (wt.%)
Station
PR02 (493 mbsl)
PR05 (1,902 mbsl)
PR04 (2,598 mbsl)
PR06 (5,373 mbsl)
PR10 (5,434 mbsl)
PR07 (8,359 mbsl)
PR08 (8,385 mbsl)
Sediment depth (cmbsf)
0
25
50
100
250
500
750
1000
1500
2000

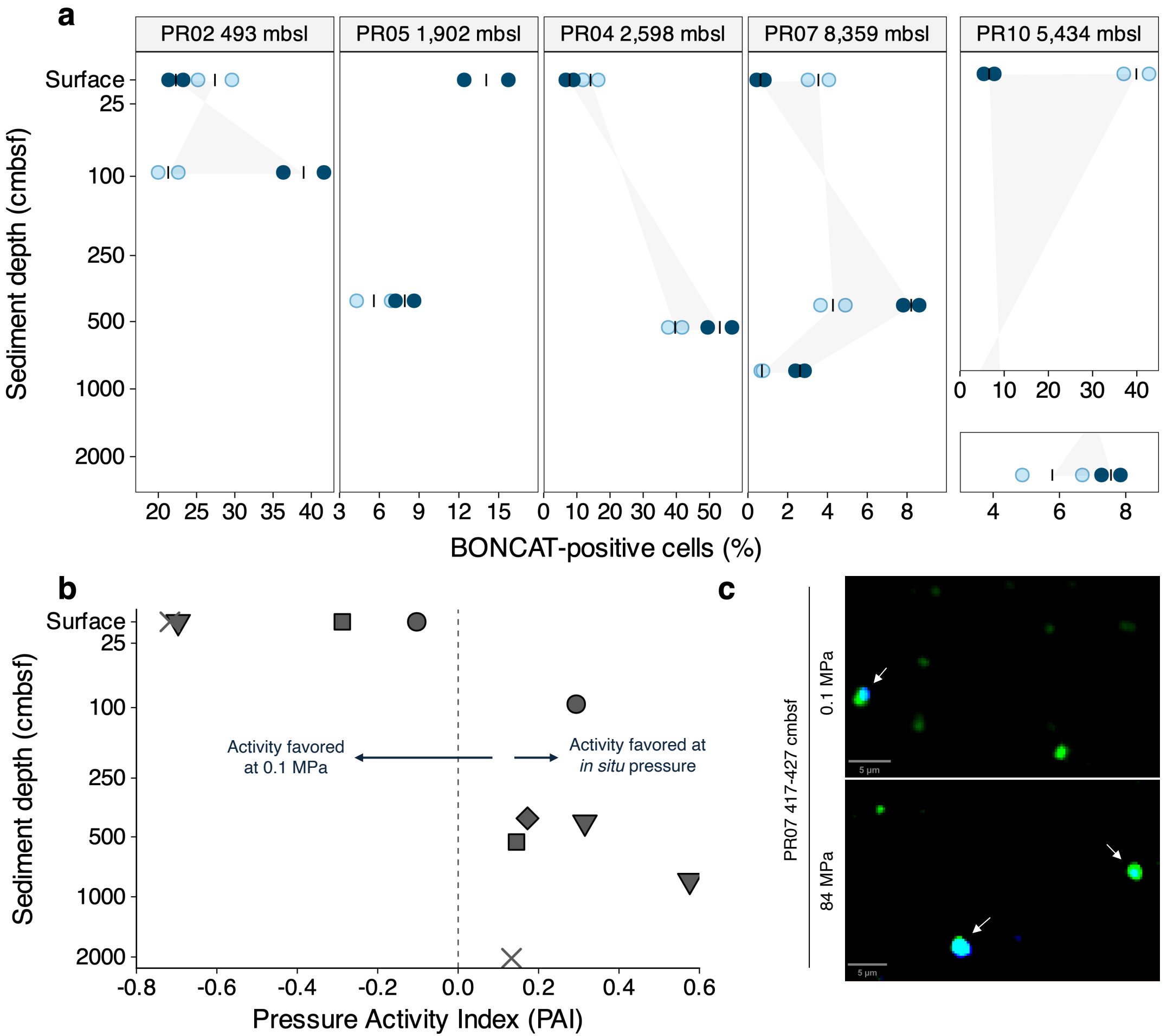

a
Assay
substrate amendment
Pressure treatment
Anabolic activity measurements
Multicore sampling
0–10 cmbsf
BONCAT: H-Homopropargylglycine
HPG
NanoSIMS: 15N ammonium
Atmospheric pressure
4 °C
in the dark
In situ
pressure
4 °C
in the dark
Cell separation
Click
chemistry
Fluorescence
microscopy
BONCAT-
positive cells (%)
NanoSIMS
Single-cell
15N assimilation
high
15N
low
15N

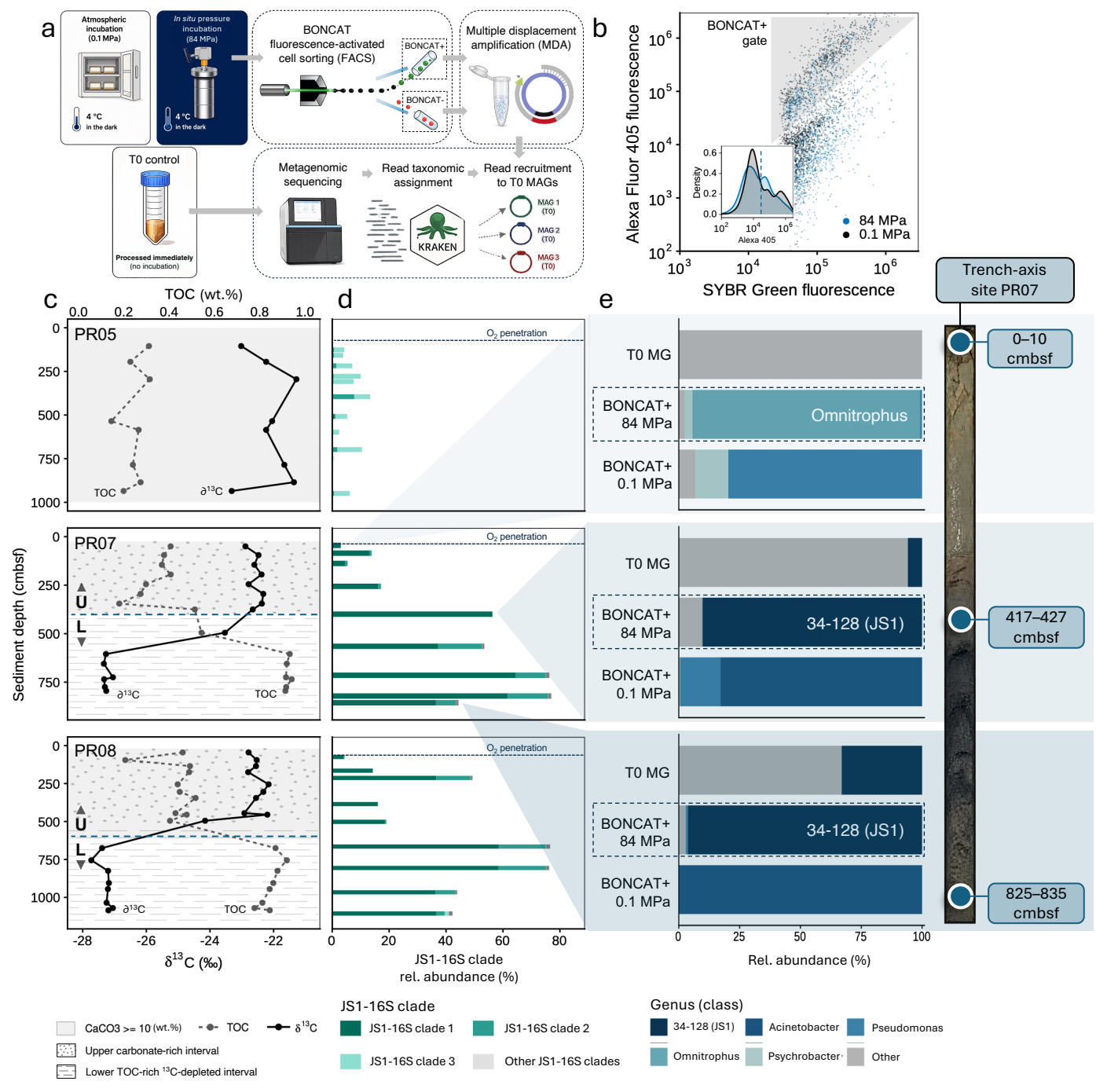

b
BONCAT-positive cells (%)
8.5 MPa
19 MPa
26 MPa
54 MPa
84 MPa
84 MPa
54 MPa
Atmospheric pressure (0.1 MPa)
in situ pressure
Margin-proximal
Bathyal slope
Abyssal slope
Hadal trench axis
Abyssal plain
PR02
493 mbsl
PR05
1,902 mbsl
PR04
2,598 mbsl
PR06
5,373 mbsl
PR07
8,359 mbsl
PR08
8,385 mbsl
PR10
5,434 mbsl
Pressure (MPa)
BONCAT+ cells (%)
Depth (m)

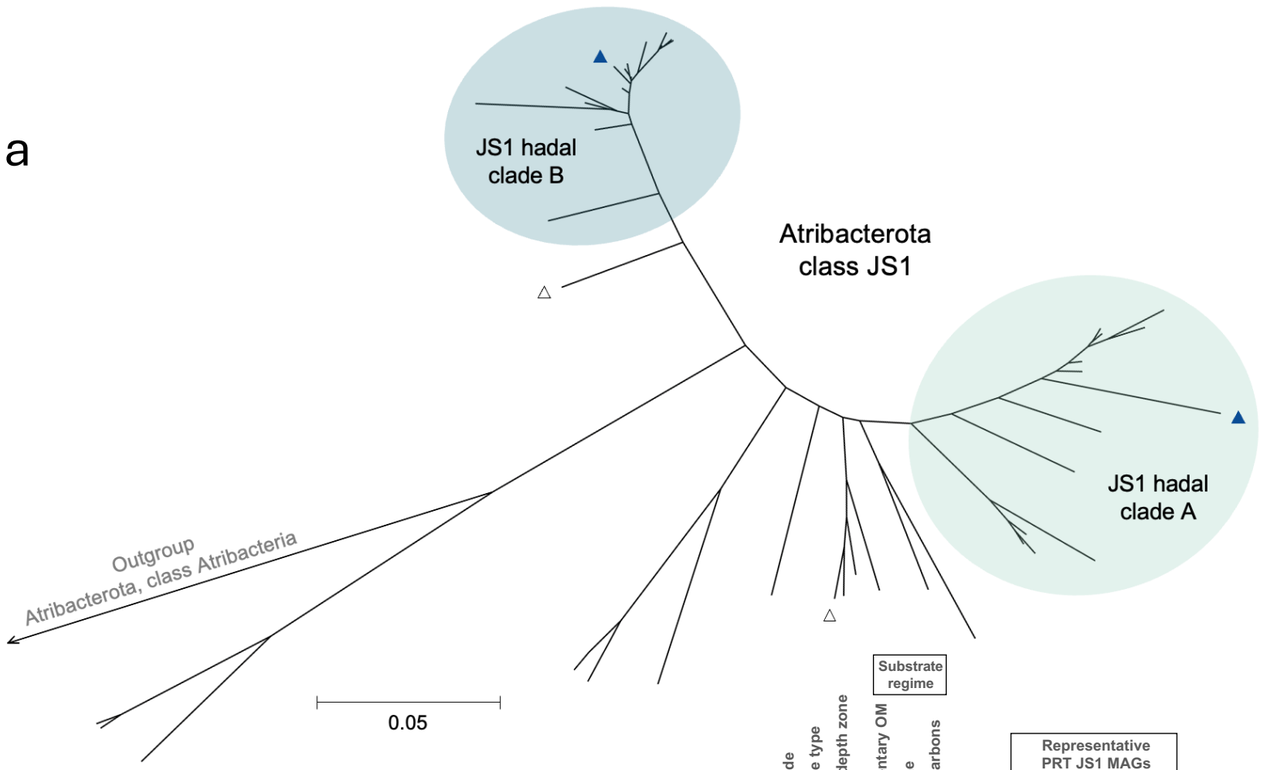

c
Pressure Activity Index (PAI)
Activity favored
at 0.1 MPa
Activity favored
at in situ pressure
PAI = (In situ − Atmospheric) / (In situ + Atmospheric)
Water depth (mbsl)

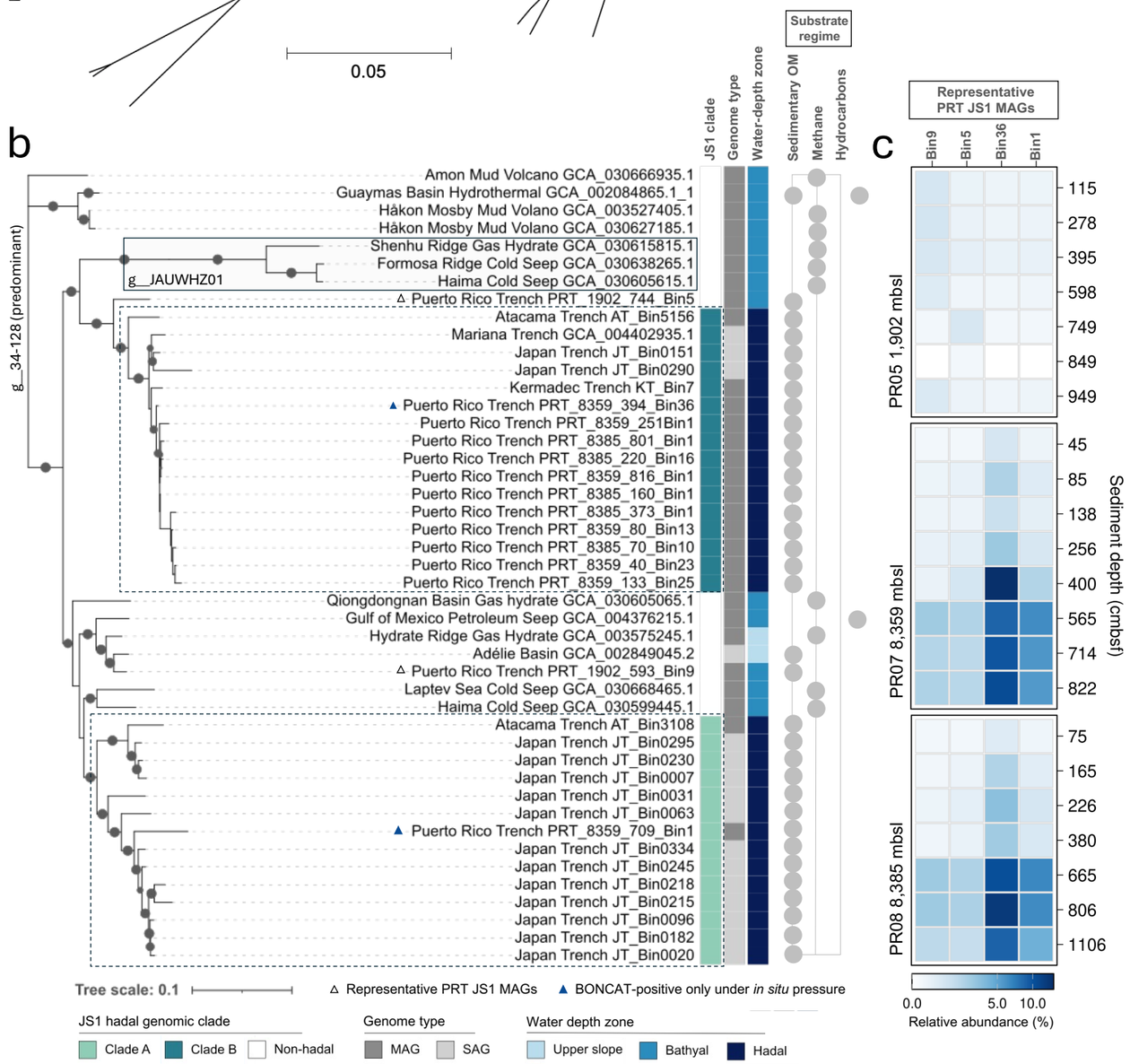

d
PR10 SYBR Green / BONCAT-Cy5
0.1 MPa
54 MPa
SYBR Green
BONCAT-Cy5
f
PR07 8,359 mbsl
PR08 8,385 mbsl
15N atom percent excess (APE)
***
P = 1.00
0.1 MPa
84 MPa
n = 228
n = 153
n = 66
n = 60
Increasing cell-to-cell heterogeneity →
Gini coefficient

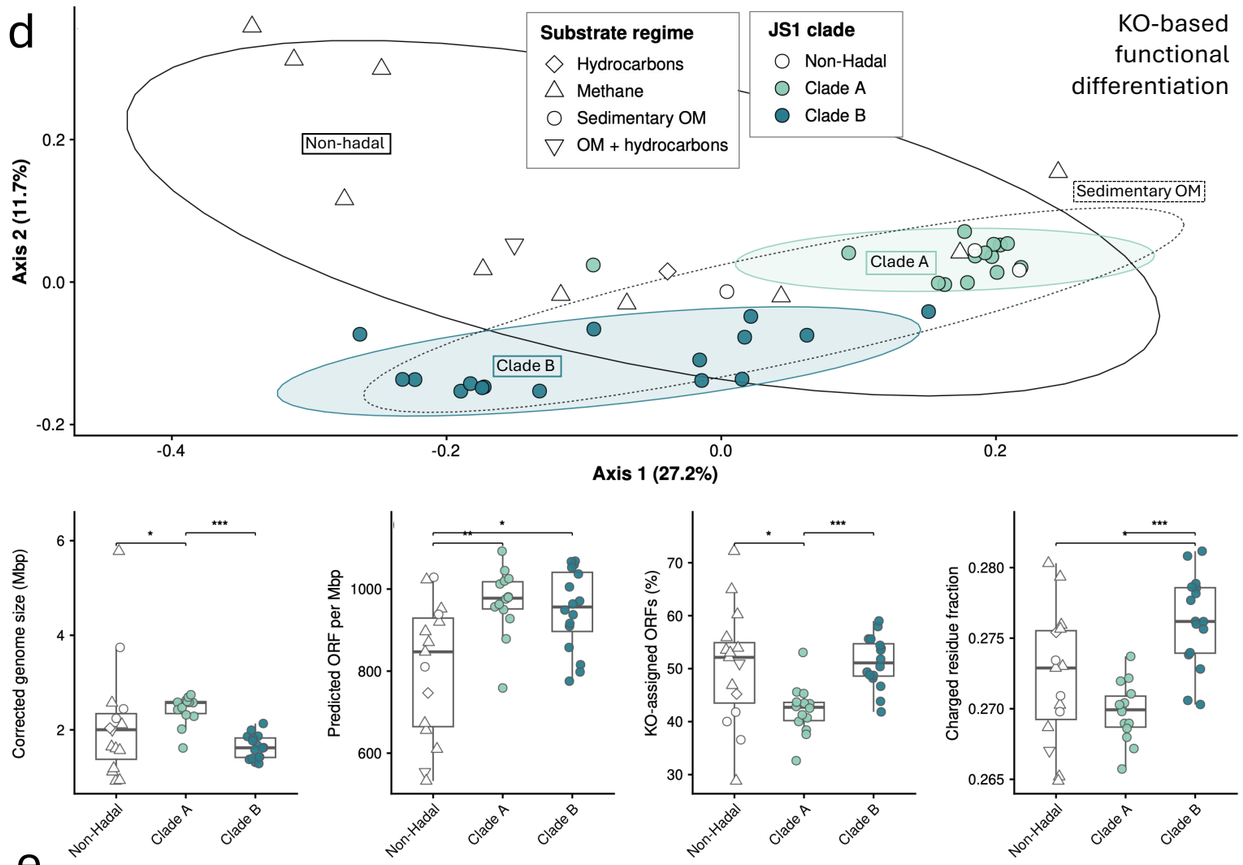

e
PR07 15N/14N
0.1 MPa
84 MPa
PR08 15N/14N
0.1 MPa
84 MPa
15N/14N
9x10-3
7x10-3
5x10-3

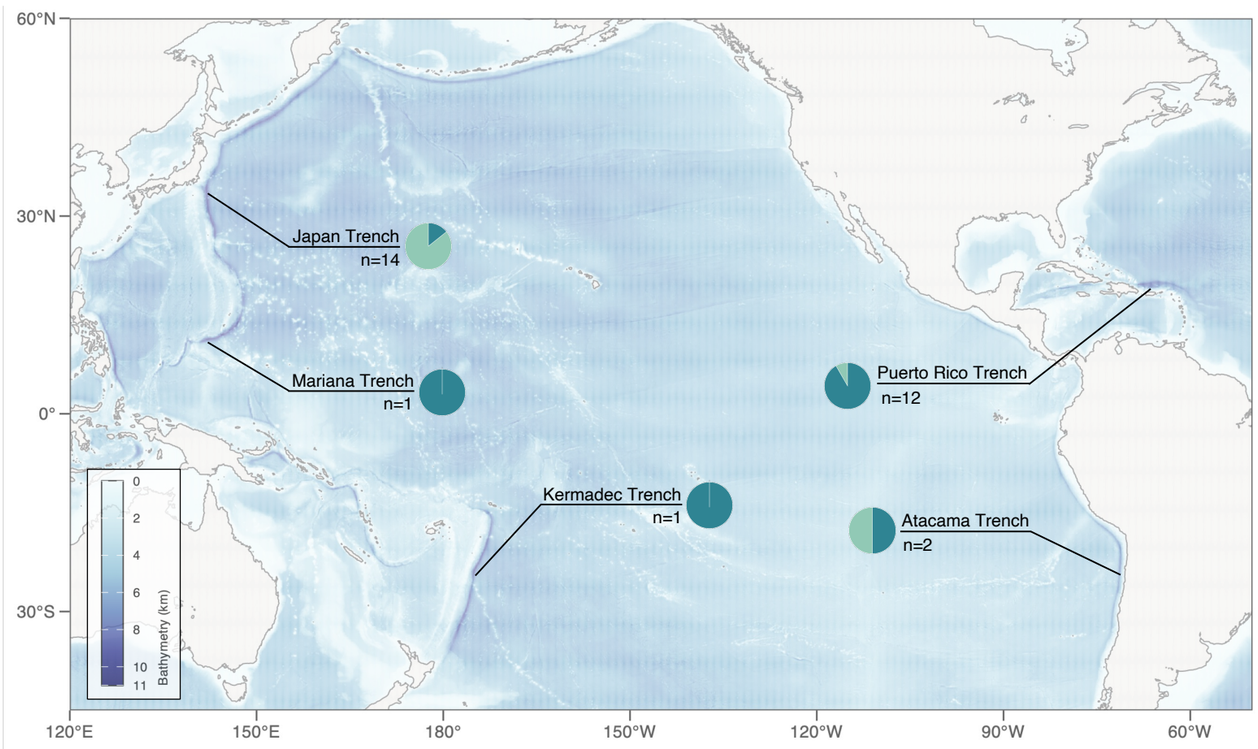

a
PR02 493 mbsl
PR05 1,902 mbsl
PR04 2,598 mbsl
PR07 8,359 mbsl
PR10 5,434 mbsl
Sediment depth (cmbsf)
Surface
25
100
250
500
1000
2000
20 25 30 35 40
3 6 9 12 15
0 10 20 30 40 50
0 2 4 6 8
0 10 20 30 40
4 6 8
BONCAT-positive cells (%)
b
Surface
25
100
250
500
1000
2000
Sediment depth (cmbsf)
Activity favored at 0.1 MPa
Activity favored at in situ pressure
-0.8 -0.6 -0.4 -0.2 0.0 0.2 0.4 0.6
Pressure Activity Index (PAI)
c
PR07 417-427 cmbsf
0.1 MPa
84 MPa
5 µm
5 µm
Pressure treatment
Atmospheric pressure (0.1 MPa)
In situ pressure
Station
PR02
PR04
PR10
PR05
PR07


a
Atmospheric incubation (0.1 MPa)
4 °C in the dark
In situ pressure incubation (84 MPa)
4 °C in the dark
BONCAT fluorescence-activated cell sorting (FACS)
BONCAT+
BONCAT-
Multiple displacement amplification (MDA)
T0 control
Processed immediately (no incubation)
Metagenomic sequencing
Read taxonomic assignment
KRAKEN
Read recruitment to T0 MAGs
MAG 1 (T0)
MAG 2 (T0)
MAG 3 (T0)
b
BONCAT+ gate
Alexa Fluor 405 fluorescence
SYBR Green fluorescence
Density
Alexa 405
84 MPa
0.1 MPa
c
TOC (wt.%)
PR05
TOC
∂13C
PR07
PR08
U
L
Sediment depth (cmbsf)
δ13C (‰)
d
O2 penetration
JS1-16S clade rel. abundance (%)
e
Trench-axis site PR07
0–10 cmbsf
417–427 cmbsf
825–835 cmbsf
T0 MG
BONCAT+ 84 MPa
BONCAT+ 0.1 MPa
Omnitrophus
34-128 (JS1)
Rel. abundance (%)
CaCO3 >= 10 (wt.%)
TOC
δ13C
Upper carbonate-rich interval
Lower TOC-rich 13C-depleted interval
JS1-16S clade
JS1-16S clade 1
JS1-16S clade 2
JS1-16S clade 3
Other JS1-16S clades
Genus (class)
34-128 (JS1)
Acinetobacter
Pseudomonas
Omnitrophus
Psychrobacter
Other


a
JS1 hadal clade B
Atribacterota class JS1
JS1 hadal clade A
Outgroup
Atribacterota, class Atribacteria
0.05


b
JS1 clade
Genome type
Water-depth zone
Substrate regime
Sedimentary OM
Methane
Hydrocarbons
Amon Mud Volcano GCA_030666935.1
Guaymas Basin Hydrothermal GCA_002084865.1_1
Håkon Mosby Mud Volano GCA_003527405.1
Håkon Mosby Mud Volano GCA_030627185.1
Shenhu Ridge Gas Hydrate GCA_030615815.1
Formosa Ridge Cold Seep GCA_030638265.1
Haima Cold Seep GCA_030605615.1
g__JAUWHZ01
Puerto Rico Trench PRT_1902_744_Bin5
Atacama Trench AT_Bin5156
Mariana Trench GCA_004402935.1
Japan Trench JT_Bin0151
Japan Trench JT_Bin0290
Kermadec Trench KT_Bin7
Puerto Rico Trench PRT_8359_394_Bin36
Puerto Rico Trench PRT_8359_251Bin1
Puerto Rico Trench PRT_8385_801_Bin1
Puerto Rico Trench PRT_8385_220_Bin16
Puerto Rico Trench PRT_8359_816_Bin1
Puerto Rico Trench PRT_8385_160_Bin1
Puerto Rico Trench PRT_8385_373_Bin1
Puerto Rico Trench PRT_8359_80_Bin13
Puerto Rico Trench PRT_8385_70_Bin10
Puerto Rico Trench PRT_8359_40_Bin23
Puerto Rico Trench PRT_8359_133_Bin25
Qiongdongnan Basin Gas hydrate GCA_030605065.1
Gulf of Mexico Petroleum Seep GCA_004376215.1
Hydrate Ridge Gas Hydrate GCA_003575245.1
Adélie Basin GCA_002849045.2
Puerto Rico Trench PRT_1902_593_Bin9
Laptev Sea Cold Seep GCA_030668465.1
Haima Cold Seep GCA_030599445.1
Atacama Trench AT_Bin3108
Japan Trench JT_Bin0295
Japan Trench JT_Bin0230
Japan Trench JT_Bin0007
Japan Trench JT_Bin0031
Japan Trench JT_Bin0063
Puerto Rico Trench PRT_8359_709_Bin1
Japan Trench JT_Bin0334
Japan Trench JT_Bin0245
Japan Trench JT_Bin0218
Japan Trench JT_Bin0215
Japan Trench JT_Bin0096
Japan Trench JT_Bin0182
Japan Trench JT_Bin0020
g__34-128 (predominant)
c
Representative PRT JS1 MAGs
Bin9
Bin5
Bin36
Bin1
PR05 1,902 mbsl
PR07 8,359 mbsl
PR08 8,385 mbsl
115
278
395
598
749
849
949
45
85
138
256
400
565
714
822
75
165
226
380
665
806
1106
Sediment depth (cmbsf)
0.0
5.0
10.0
Relative abundance (%)
Tree scale: 0.1
Representative PRT JS1 MAGs
BONCAT-positive only under in situ pressure
JS1 hadal genomic clade
Clade A
Clade B
Non-hadal
Genome type
MAG
SAG
Water depth zone
Upper slope
Bathyal
Hadal


d
KO-based functional differentiation
Substrate regime
Hydrocarbons
Methane
Sedimentary OM
OM + hydrocarbons
JS1 clade
Non-Hadal
Clade A
Clade B
Non-hadal
Sedimentary OM
Clade A
Clade B
Axis 2 (11.7%)
Axis 1 (27.2%)
Corrected genome size (Mbp)
Predicted ORF per Mbp
KO-assigned ORFs (%)
Charged residue fraction
Non-Hadal
Clade A
Clade B


e
Japan Trench
n=14
Mariana Trench
n=1
Puerto Rico Trench
n=12
Kermadec Trench
n=1
Atacama Trench
n=2
Bathymetry (km)
60°N
30°N
0°
30°S
120°E
150°E
180°
150°W
120°W
90°W
60°W